

Beyond fragmented dopant dynamics in quantum spin lattices: Robust localization and sub-diffusion

Mingru Yang,^{1,2} Sajant Anand,^{3,4} and Kristian Knakkegaard Nielsen^{5,1}

¹Max Planck Institute of Quantum Optics, Hans-Kopfermann-Str. 1, D-85748 Garching, Germany

²Munich Center for Quantum Science and Technology, Schellingstraße 4, 80799 München, Germany

³Department of Physics, University of California, Berkeley, CA 94720, USA

⁴Material Science Division, Lawrence Berkeley National Laboratory, Berkeley, California 94720, USA

⁵Niels Bohr Institute, University of Copenhagen, Jagtvej 128, DK-2200 Copenhagen, Denmark

(Dated: July 23, 2025)

The motion of dopants in magnetic spin lattices has received tremendous attention for at least four decades due to its connection to high-temperature superconductivity. Despite these efforts, we lack a complete understanding of their behavior, especially out-of-equilibrium and at nonzero temperatures. In this Article, we take a significant step towards a much deeper understanding based on state-of-the-art matrix-product-state calculations. In particular, we investigate the non-equilibrium dynamics of a dopant in two-leg t - J ladders with antiferromagnetic XXZ spin interactions. In the Ising limit, we find that the dopant is *localized* for all investigated *nonzero* temperatures due to an emergent disordered potential, with a localization length controlled by the underlying correlation length of the spin lattice, whereby it only delocalizes asymptotically in the zero temperature limit. This greatly generalizes the localization effect discovered recently in Hilbert space fragmented models [1, 2]. In the presence of spin-exchange processes, the dopant delocalizes according to a power-law behavior, which is strongly sub-diffusive for weak spin-exchange but which eventually becomes diffusive for strong enough exchange. Moreover, we show that the underlying spin dynamics at infinite temperature behaves qualitatively the same, albeit with important quantitative differences. We substantiate these findings by showing that the dynamics shows self-similar scaling behavior, which strongly deviates from the Gaussian behavior of regular diffusion. Finally, we show that the diffusion coefficient follows an Arrhenius relation at high temperatures, whereby it exponentially decreases for decreasing temperatures.

I. INTRODUCTION

Tremendous effort has been dedicated to the study of emergent many-body properties at low energy and in equilibrium. While generic quantum many-body systems are exponentially complex in system size, static and local interactions at low energies typically lead to states with only area-law entanglement [3, 4]. This emergent structure has enabled the success of tensor network algorithms [5]. In recent years, however, quantum simulators have pushed beyond this regime and, e.g., investigated dynamical phase transitions [6, 7], quantum many-body scars [8, 9] and Hilbert space fragmentation [10, 11]. This has unveiled that emergent structures are not limited to low energies and equilibrium; they may appear dynamically and throughout the many-body spectrum as well.

For ultracold atoms in optical lattices in particular, the awesome capabilities of single-site resolved quantum gas microscopy [12–17] call for more precise theoretical descriptions of the rich behaviors in the dynamics of local observables. More specifically, such systems naturally implement Fermi-Hubbard and t - J models [18–20] and allow us to probe the intricate interplay of charge and spin degrees of freedom [21–28], which is at the core of our understanding of strongly correlated electronic systems, including high-temperature superconductors [29].

A central interest in this respect is to study with great detail the microscopic behavior of charges (dopants) both in [30, 31] and out of equilibrium [32]. It is generally

believed that dopant motion leads to the formation of itinerant quasiparticles [33, 34], which is also consistent with experiments so far [35]. There is currently, however, still no explicit evidence for their existence [36]. This is echoed on the theoretical side, where we have so far lacked high-accuracy results. For example, it is not clear whether quasiparticles are present in general t - J models [37–42], although matrix product state (MPS) calculations have shown robust magnetic polaron quasiparticles in ladders [40] and quasi one-dimensional (1D) cylindrical geometries at *zero* temperature [43], leading to ballistic transport of dopants. At nonzero temperatures, thermal damping is expected to break this quasiparticle behavior. Indeed, initial studies at *infinite* temperatures in two-dimensional (2D) square lattices revealed slower than ballistic behavior [44, 45], though the actual long-time behavior remains illusive.

Understanding the temperature dependence of dopant dynamics, therefore, remains an outstanding and fundamental challenge. In this work, we address this issue by investigating a minimal setup of two-leg t - J ladders with antiferromagnetic XXZ spin interactions [Fig. 1(a)]. We generalize a previously studied Hilbert space fragmented model [Fig. 1(b)], in which dopants are localized at any nonzero temperature and spin interaction [1]. In the Ising limit, we show that localization is robust, even though fragmentation breaks down, and find that the localization length scales with the underlying spin-spin correlation length. For weak spin-exchange processes

ories with static charges [49, 50]. Indeed, both systems can be mapped to an Anderson model of free fermions with onsite disorder [51], utilizing the underlying Hilbert space fragmentation of the respective models [52]. A natural question to ask, therefore, is:

Is the localization mechanism tied to Hilbert space fragmentation?

I.e., does localization only happen in the fragmented models, or is it possible to retain localization in more generic situations? Moreover, what kind of transport behavior do we expect if localization breaks down when the Hilbert space is no longer fragmented? Will the dopants, e.g., immediately start to diffuse?

To simplify the problem but still retain the essential 2D physics, we focus our studies on a minimal two-leg $N_x \times 2$ ladder geometry subject to the t - J Hamiltonian

$$\hat{H} = \hat{H}_t + \hat{H}_J = - \sum_{\substack{\lambda=\parallel,\perp \\ \sigma=\uparrow,\downarrow}} \sum_{\langle \mathbf{i}, \mathbf{j} \rangle_\lambda} t_\lambda \hat{P} \left[\hat{c}_{\mathbf{i}\sigma}^\dagger \hat{c}_{\mathbf{j}\sigma} + \hat{c}_{\mathbf{j}\sigma}^\dagger \hat{c}_{\mathbf{i}\sigma} \right] \hat{P} + J \sum_{\langle \mathbf{i}, \mathbf{j} \rangle} \left[\hat{S}_\mathbf{i}^z \hat{S}_\mathbf{j}^z + \alpha \left(\hat{S}_\mathbf{i}^x \hat{S}_\mathbf{j}^x + \hat{S}_\mathbf{i}^y \hat{S}_\mathbf{j}^y \right) \right]. \quad (3)$$

This describes nearest-neighbor (NN) constrained hoppings t_\parallel, t_\perp , of spin-1/2 fermions interacting via anti-ferromagnetic XXZ-type NN spin interactions $J > 0$ [Fig. 1(a)]. Indeed, $\hat{c}_{\mathbf{i}\sigma}^\dagger$ ($\hat{c}_{\mathbf{i}\sigma}$) creates (destroys) a fermion at site \mathbf{i} with spin- z $\sigma = \uparrow, \downarrow$, while \hat{P} projects onto the subspace of at most one fermion per site. In experiments, such models may naturally be implemented by combining Fermi-Hubbard simulators using ultracold atoms in optical lattices [21–28, 30–32] with Rydberg dressing [53, 54], or alternatively using dipole-dipole and van der Waals interactions in Rydberg arrays [55, 56]. Our findings are, therefore, not only fundamentally important for understanding these systems, but may also be tested in state-of-the-art quantum simulators.

The aforementioned fragmented t - J_z limit is recovered when both the rung hopping and the spin anisotropy vanish, $t_\perp = \alpha = 0$. We then consider two *distinct* ways of breaking fragmentation: (1) a nonzero rung hopping, $t_\perp > 0$, and (2) a nonzero spin anisotropy, $\alpha > 0$. In the latter case, the ensuing spin exchange connects all spin configurations with the same conserved quantum numbers, N_\uparrow, N_\downarrow . In the former case with Ising interactions, nonzero hopping along both spatial directions has the same effect and is rooted in the possibility of moving in loops in the lattice [44, 57]. In turn, both scenarios ($t_\perp > 0$ and $\alpha > 0$) break Hilbert space fragmentation, in that the many Krylov sub-sectors for given N_\uparrow, N_\downarrow now implode to one single $U(1)$ block [Fig. 1(c)].

One might expect that localization breaks down in both cases, because the system is now in principle *ergodic*. However, we show that the two scenarios play out in drastically distinct ways. For the t - J_z limit with nonzero *rung hopping* t_\perp , we show that localization re-

mains at all investigated *nonzero* temperatures and that the basic mechanism in terms of an emergent disordered energy landscape is upheld. However, for nonzero spin exchange processes $\propto \alpha J$, the ensuing transport of *spins* immediately leads to delocalization of dopants. Furthermore, we give strong numerical evidence that there is a continuous crossover from localized to sub-diffusive to diffusive transport of dopants, following an α -dependent power-law behavior $\sim \tau^{1/z(\alpha)}$, with the limiting values of the dynamical exponent being $1/z(\alpha = 0) = 0$ and $1/z(\alpha \gtrsim 0.3) = 1/2$. These results are summarized in the high-temperature dynamical phase diagram in Fig. 1(d) and imply that the dopant only thermalizes with its spin environment away from the Ising limit of $\alpha = 0$.

III. SETUP AND METHODS

To track the non-equilibrium dynamics of a single dopant at temperature $k_B T = 1/\beta$, we initialize the system with one spin per site (half filling) in a thermal Gibbs state of the spins, $\hat{\rho}_J = \exp(-\beta \hat{H}_J)/Z_J$ with $Z_J = \text{tr}[\exp(-\beta \hat{H}_J)]$ being the spin partition function of the canonical ensemble. We then create a single hole at the origin (bottom site of left-most rung),

$$\hat{\rho}(0) = \sum_{\sigma_0} \hat{c}_{0,\sigma_0} \hat{\rho}_J \hat{c}_{0,\sigma_0}^\dagger, \quad (4)$$

and time evolve it. In order to calculate the expectation value of some time-evolved observable, $\hat{A}(\tau) = \exp(+i\hat{H}\tau) \hat{A} \exp(-i\hat{H}\tau)$, we sample the thermal ensemble through the minimally entangled typical thermal state (METTS) [58] approach, i.e.

$$\begin{aligned} \langle \hat{A}(\tau) \rangle &= \text{tr}[A(\tau) \hat{\rho}(0)] = \sum_{\sigma_0} \text{tr}[e^{+i\hat{H}\tau} \hat{A} e^{-i\hat{H}\tau} \hat{c}_{0,\sigma_0} \hat{\rho}_J \hat{c}_{0,\sigma_0}^\dagger] \\ &= \frac{1}{Z_J} \sum_{\sigma_0} \sum_{\boldsymbol{\sigma}} p(\boldsymbol{\sigma}) \langle \phi_{\sigma_0}(\boldsymbol{\sigma}, \tau) | \hat{A} | \phi_{\sigma_0}(\boldsymbol{\sigma}, \tau) \rangle. \end{aligned} \quad (5)$$

Consequently, $\langle \hat{A}(\tau) \rangle$ is computed as the statistical average over the sample states

$$|\phi_{\sigma_0}(\boldsymbol{\sigma}, \tau)\rangle = e^{-i\hat{H}\tau} \hat{c}_{0,\sigma_0} |\phi(\boldsymbol{\sigma})\rangle \quad (6)$$

according to the probability distribution $p(\boldsymbol{\sigma})/Z_J$, with $p(\boldsymbol{\sigma}) = \langle \boldsymbol{\sigma} | \exp(-\beta \hat{H}_J) | \boldsymbol{\sigma} \rangle$ the unnormalized probability for the initial thermal state to be in the product spin state $|\boldsymbol{\sigma}\rangle = \otimes_{\mathbf{i}} |\sigma_{\mathbf{i}}\rangle$. Note that we use τ as the time variable to distinguish it from the hopping amplitude t_\parallel, t_\perp . To prepare $|\phi_{\sigma_0}(\boldsymbol{\sigma}, \tau)\rangle$, we, thus, first imaginary-time evolve a sampled product state to obtain a METTS, i.e. $|\phi(\boldsymbol{\sigma})\rangle = p(\boldsymbol{\sigma})^{-1/2} \exp(-\beta \hat{H}_J/2) |\boldsymbol{\sigma}\rangle$, then remove a spin σ_0 from the origin, $\mathbf{0}$, and finally real-time evolve it to time τ . The imaginary and real time evolution are performed using the time-dependent variational principle (TDVP) [59–61] and the time evolving block decimation (TEBD) [62, 63], respectively. For TEBD, we use SWAP

gates to switch the interacting sites in the two-leg ladder geometry to nearest neighbor in MPS [40]. See App. B for more details. To achieve *high-accuracy* and *unbiased* results, we generally fix the maximum truncation error in each time step and let the bond dimension grow freely. The product states $|\sigma\rangle$ in METTS can be sampled by generating a Markov chain through an efficient state-collapse step [64]. In the Ising limit, $\alpha = 0$, one can further simplify the sampling, because now $p(\sigma) = \exp(-\beta E_J(\sigma))$, where $E_J(\sigma)$ is the magnetic energy of the Ising state $|\sigma\rangle$. Thus, one can use regular Metropolis-Hasting algorithms [65, 66] for the sampling in this limit.

The bulk of the analysis focuses on the dynamics of the hole density, setting $\hat{A} = \hat{n}_h(\mathbf{i}) = 1 - \sum_{\sigma} \hat{c}_{i\sigma}^{\dagger} \hat{c}_{i\sigma}$, and the main observable is the root-mean-square (rms) distance of the hole to its origin, $\mathbf{i}_0 = \mathbf{0}$ (included here for conceptual clarity),

$$d_{\text{rms}}(\tau) = \left[\sum_{\mathbf{i}} (\mathbf{i} - \mathbf{i}_0)^2 n_h(\mathbf{i}, \tau) \right]^{1/2}, \quad (7)$$

with $n_h(\mathbf{i}, \tau) = \langle \hat{n}_h(\mathbf{i}, \tau) \rangle$. Therefore, localization corresponds to a bounded rms distance, $d_{\text{rms}}(\tau) \leq C$ for all τ , whereas ballistic and diffusive motion manifests as $d_{\text{rms}}(\tau) \propto \tau$ and $d_{\text{rms}}(\tau) \propto \tau^{1/2}$, respectively, for $\tau \rightarrow \infty$. We choose to initialize the dopant at the left end of the two-leg ladder to minimize the required system sizes. While this certainly results in boundary effects at short times, it does *not* alter the nature of the long-time propagation, i.e. whether it is ballistic, diffusive, sub-diffusive or localized. We also note that at sufficiently short times, $t_{\parallel} \tau, t_{\perp} \tau \ll 1$, the dopant *always* moves independently of the spin background with the ballistic speed of a free particle with nearest neighbor hopping amplitudes t_{\parallel}, t_{\perp} [35], such that $d_{\text{rms}}(\tau) = [t_{\parallel}^2 + t_{\perp}^2]^{1/2} \times \tau$ in this regime.

IV. ISING LIMIT

We start our analysis in the Ising limit and investigate the impact of turning on the rung hopping t_{\perp} . To this end, we compare the ensuing dynamics of placing the dopant at the left end of the ladder in the zero temperature Néel ground state to the infinite temperature behavior of completely randomized spins.

For $t_{\perp} = 0$, the dopant can only move the spin pattern in the bottom leg one site to the left as shown by the black long-dashed box in Figs. 2(a) and 2(f). At zero temperature, dopant motion in the Néel ground state, $|\psi_{\text{N}}\rangle$, leads to l pairs of spins that go from being anti-aligned with energy $-J/4$ to aligned with energy $+J-4$ after a traveled distance of l along each passed rung [see Fig. 2(b)]. As a result, the total magnetic energy change is $E_J(l) = \langle \psi_{\text{N}}(l) | \hat{H}_J | \psi_{\text{N}}(l) \rangle - \langle \psi_{\text{N}}(0) | \hat{H}_J | \psi_{\text{N}}(0) \rangle = [J/4 - (-J/4)] \times l = J/2 \times l$ [67]. Here, $|\psi_{\text{N}}(l)\rangle$ denotes the state after the dopant has hopped l times along the

straight path above Fig. 2(b). Any $t_{\perp} > 0$ enables Trugman loops [68]. Indeed, when the dopant makes 6 hops counter-clockwise around a 2×2 plaquette, all spins are moved clockwise by 2 sites. Performing several of such loops consecutively [green arrows around numbered plaquettes in Fig. 2(a)] moves the entire staggered magnetization pattern one rung to the left and flips it upside down. For a Néel ground state, the associated magnetic energy $E_J(l)$ along such a path is periodic with a periodicity of 6. As a result, the dopant delocalizes, as shown in Fig. 2(d), where the rms distance of the dopant to its initial position eventually grows linearly at long times as the rung hopping is increased. We note, however, that the long-time propagation speed strongly depends on t_{\perp} , such that the data for $t_{\perp} = 0.2, 0.4$ still shows only very small propagation distances on the plotted timescales. Interestingly, the probability of the dopant to return to its origin, $n_h(\mathbf{i} = \mathbf{0}, \tau)$, in Fig. 2(e) remains high, showing that the dopant density profile has a localized core and delocalized wings.

At infinite spin temperatures, the dopant moving in a lattice with $t_{\perp} = 0$ leads to a *disordered* magnetic energy landscape, as shown in Fig. 2(g). Here, we plot the magnetic energy $E_J(\sigma, l) = \langle \psi_{\sigma}(l) | \hat{H}_J | \psi_{\sigma}(l) \rangle - \langle \psi_{\sigma}(0) | \hat{H}_J | \psi_{\sigma}(0) \rangle$ after the dopant has moved l sites along the straight path shown above Fig. 2(g) for 50 randomly chosen spin configurations σ . This disordered magnetic potential emerges because when the dopant moves along a straight path, the spins on a specific rung randomly reconfigures from being aligned to anti-aligned or vice versa [2]. This leads to disorder-induced Anderson localization [51], even though there is no quenched disorder in the Hamiltonian. As such, this phenomenon is very similar to the disorder-free localization effect discovered for lattice gauge theories with static gauge fields [49, 50]. One key difference is that the disorder strength here *increases with distance traveled*. Indeed, while the emergent magnetic potential $E_J(\sigma, l)$ experienced by the dopant on average vanishes across the spin samples, $\mu[E_J(\sigma, l)] = 0$, the standard deviation from sample to sample, $\text{std}[E_J(\sigma, l)] = (\text{Var}[E_J(\sigma, l)])^{1/2} \propto |J| \times l^{1/2}$, grows as a square root with distance l [1, 2]. This is shown in solid black lines in Fig. 2(g).

Trugman loops still move the entire spin ladder one rung to the left and flip it upside down, as shown above Fig. 2(h). Crucially, however, the magnetic energy landscape, $E_J(\sigma, l)$, experienced by the dopant along such a path *remains* disordered, although the disorder strength now becomes *bounded* as a function of distance [Fig. 2(h)]. As a result, even though the system is no longer fragmented, the dopant remains localized for any rung hopping, as shown by the finite rms distance in Fig. 2(i) and in stark contrast to the zero-temperature behavior. The dopant is, nevertheless, seen to spread out more for increasing t_{\perp} . Moreover, the dynamics also has a slower approach to its final steady state. As a direct result of the localization, the return probability in Fig. 2(j) remains nonzero. In turn, this localization effect implies

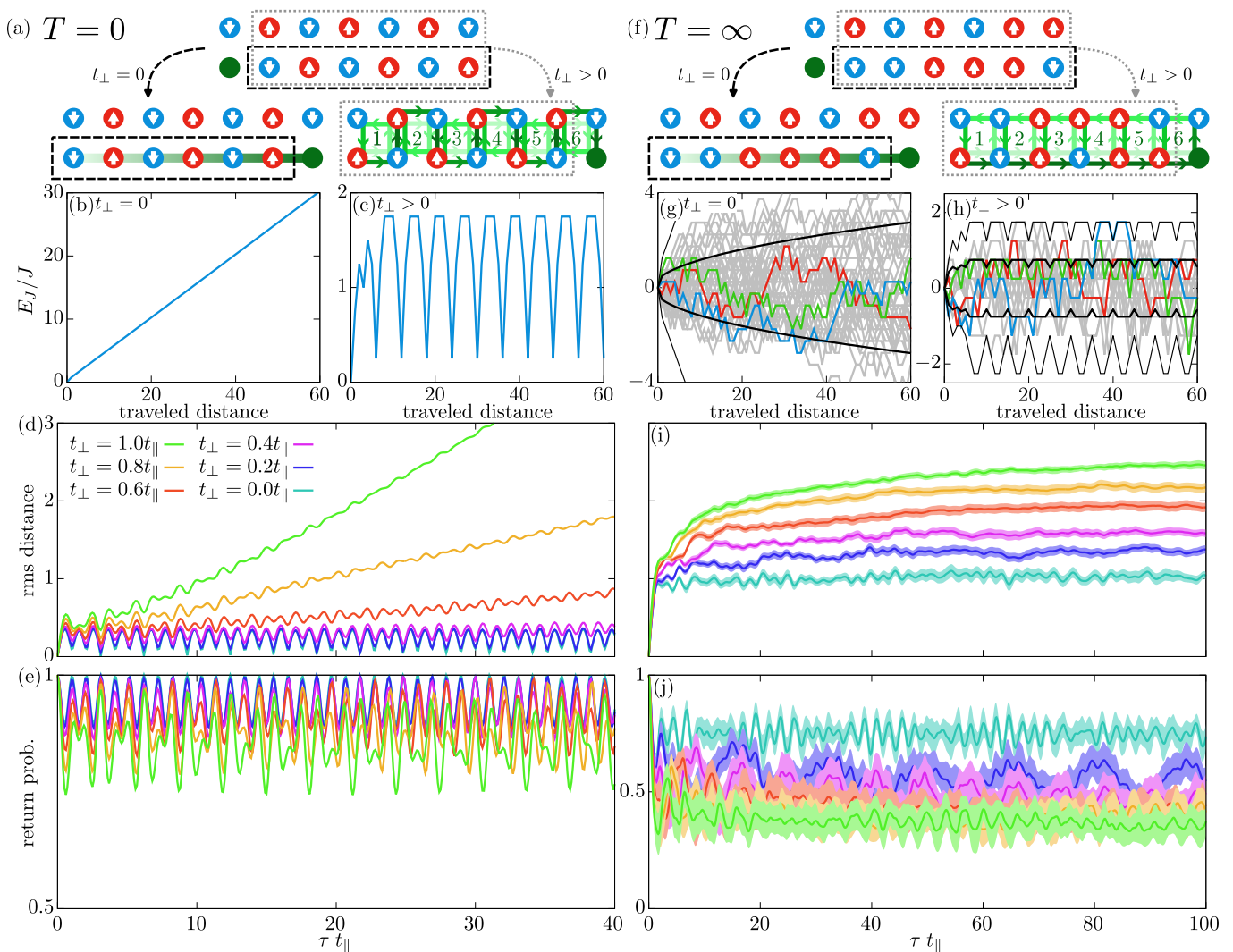


FIG. 2. **Dopant dynamics in the Ising limit.** Dopant dynamics at zero temperature (a)-(e), and infinite temperature (f)-(j) in the Ising limit ($\alpha = 0$) for indicated values of the rung hopping and $J = 8t_{\parallel}$. (a) and (f) For $t_{\perp} = 0$, the spins can only move one site to the left [black long-dashed box]. $t_{\perp} > 0$ enables Trugman loops shown by the light to dark green arrows around numbered (1-6) 2×2 plaquettes. This moves the entire spin pattern one rung to the left and flips it on its head. (b),(c) Magnetic energy experienced along the specified paths in the zero temperature Néel ground state. (g),(h) Magnetic energy along the specified paths at *infinite temperature* shown for 50 spin realizations (gray lines), with three highlighted in color (red, blue and green lines). Thick black lines show the standard deviation, $\text{std}(E_J)$, averaged over all spin configurations. Thin black lines show the minimal and maximal values of E_J . (d),(i) Resulting rms distance dynamics of the dopant featuring long-time ballistic behavior at zero temperature and robust localization at infinite temperature as the rung hopping is turned on. (e),(j) In both cases, the probability of the dopant returning to the origin remains nonzero. Shaded areas show the estimated standard errors on the mean from the 200 samples of the spin background. In the TEBD calculations, we use a maximum truncation error of 10^{-8} and a system sizes of $N_x \times N_y = 61 \times 2$ ($T = 0$) and $N_x \times N_y = 25 \times 2$ ($T = \infty$).

that the dopant retains a memory of its initial state and cannot thermalize with its spin environment.

A. Temperature dependency

We end our analysis of the Ising limit by investigating how susceptible the localization effect is to lowering the temperature away from $T = \infty$. To this end, we perform classical Monte-Carlo sampling of the thermal spin back-

ground and again calculate the subsequent quantum dynamics using TEBD, as described by Eq. (5). The resulting rms dynamics of the dopant is given in Fig. 3(a) in the case of $t_{\perp} = t_{\parallel}$, which shows persistent localization for all the investigated nonzero temperatures. We also note that at intermediate timescales a ballistic regime appears with a propagation speed in good agreement with the zero-temperature limit. Long-lived quasiparticles (magnetic polarons), hereby, emerge in the low-temperature regime, which, however, eventually dampen out for all the investigated nonzero temperatures and gives way to

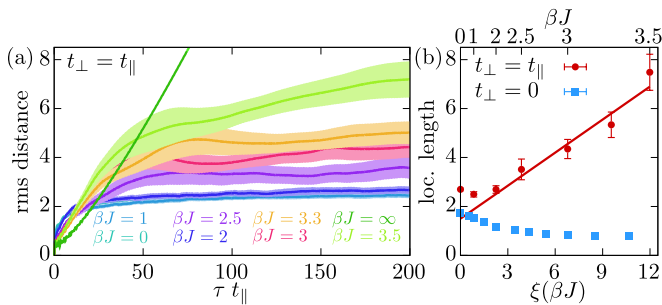


FIG. 3. **Temperature dependence of localization.** (a) Dopant rms dynamics for indicated inverse temperatures, $t_{\perp} = t_{\parallel}$ and $J = 8t_{\parallel}$ showing persistent localization at any nonzero temperature. Moreover, a ballistic regime appears at intermediate timescales $\tau t_{\parallel} \sim 10$ for the lowest nonzero temperatures. This indicates the emergence of quasiparticles, here with lifetimes $\sim 20/t_{\parallel}$. Shaded areas show estimated standard errors on the mean from 200 spin samples. For the TEBD, we use a truncation error of 10^{-8} and system sizes ranging from $N_x \times N_y = 45 \times 2$ ($\beta J = 1$) to $N_x \times N_y = 161 \times 2$ ($\beta J = 3.5$). (b) Corresponding localization length for indicated t_{\perp} versus the inverse temperature (top axis) as well as the underlying spin-spin correlation length $\xi(\beta J)$ (bottom axis), revealing a linear dependency (red line) for $t_{\perp} = t_{\parallel}$ and a saturating localization length (blue line) for $t_{\perp} = 0$.

localized behavior on longer timescales. For $t_{\perp} > 0$, the associated localization length [Fig. 3(b)],

$$l_{\text{loc}} = \lim_{\tau \rightarrow \infty} d_{\text{rms}}(\tau), \quad (8)$$

shows linear scaling with the underlying correlation length

$$\xi(\beta J) = \left[-\frac{\beta|J|}{4} + \ln \left(\coth \frac{1}{2}\beta|J| \cosh \frac{1}{4}\beta|J| \right) + \sqrt{\left(\coth \frac{1}{2}\beta|J| \cosh \frac{1}{4}\beta|J| \right)^2 - 1} \right]^{-1} \quad (9)$$

of the spin-spin correlator: $\langle \hat{S}_{\mathbf{i}}^z \hat{S}_{\mathbf{i}+\mathbf{d}}^z \rangle \sim \exp(-|\mathbf{d}|/\xi)$ [1]. This is in stark contrast to the behavior for $t_{\perp} = 0$, where the localization length *decreases* with decreasing temperature [Fig. 3(b)]. For $t_{\perp} = 0$, this decrease in localization length is a result of the fact that the dopant to a larger and larger extent experiences the strongly localizing linear potential in Fig. 2(b).

To understand the linear scaling of the localization length with correlation length for $t_{\perp} > 0$, note that the dopant spreads out more and more efficiently via the Trugman loops in Fig. 2(c). This naturally leads to a localization length on the order of $\xi(\beta J)$, because $\xi(\beta J)$ sets the length scale over which the Néel antiferromagnetic pattern is upheld. In turn, it also sets the length scale over which the dopant experiences the periodic potential in Fig. 2(c). The results thus strongly suggest that the dopant delocalizes asymptotically with $\xi(\beta J) \sim \exp(\beta J)$ as $T \rightarrow 0$. We note that a completely

analogous scaling of the localization length with $\xi(\beta J)$ was previously found for *ferromagnetic* spin interactions in the limit of $t_{\perp} = 0$ [1], whose origin is similar in that the dopant becomes more and more free to move at decreasing temperatures.

V. SPIN-EXCHANGE

We now turn to analyze the dopant motion once the spin-exchange is turned on ($\alpha > 0$). To achieve long enough evolution times at nonzero temperatures, we will mostly use intermediate system sizes of $N_x \times N_y = 11 \times 2$. Throughout our analysis, we have checked that the probability to be on the right edge remains below 0.01, such that finite-size effects may still safely be ignored. Moreover, we continue to fix the maximum truncation error rather than the bond dimension to achieve highly accurate and unbiased results.

Fig. 4, hereby, compares the dynamics at zero ($T = 0$) and infinite ($T = \infty$) spin temperatures in the absence of rung hopping ($t_{\perp} = 0$). At $T = 0$ and for $0.2 \leq \alpha \leq 1$, we see a clear three-stage process in qualitative agreement with the 2D behavior found using approximate diagrammatic techniques [35]. The three-stage process consists of: (1) the dopant moves with the universal initial speed $v = t_{\parallel}$ [short-dashed line in Fig. 4(a)], (2) an intermediate oscillatory regime, before (3) a final ballistic regime sets in [long-dashed line in Fig. 4(a)]. The latter ballistic regime is due to the formation of magnetic polaron quasiparticles [40]. Though not immediately evident outside the regime of $0.2 \leq \alpha \leq 1$, we expect this to appear at sufficiently long times regardless of $\alpha > 0$. Moreover, similar to the nonzero rung hopping case, this ballistic behavior is accompanied by a remaining localized core at least at the intermediate timescales investigated here, as seen in the return probability in Fig. 4(c).

At infinite temperatures, however, there is a stark qualitative contrast to the nonzero rung hopping case in the Ising limit: after the initial universal regime with propagation speed $v = t_{\parallel}$, the dopant is now seen to delocalize on long timescales [Fig. 4(b)]. Indeed, we see a clear crossover from localized behavior in the Ising limit ($\alpha = 0$) to diffusive behavior for large enough α . This is also reflected in the power-law decay of the return probability [Fig. 4(d)]. Moreover, the overall dependency on the spin-exchange both at zero and infinite temperatures is seen to be the same. Indeed, the propagation in both cases is seen to be the fastest at intermediate values of $\alpha \simeq 0.6$.

A. Comparison to spin dynamics and self-similar scaling

Before we analyze the phenomena above in more detail, we take a step back and compute the spin dynamics in the absence of dopants to enable a direct comparison between

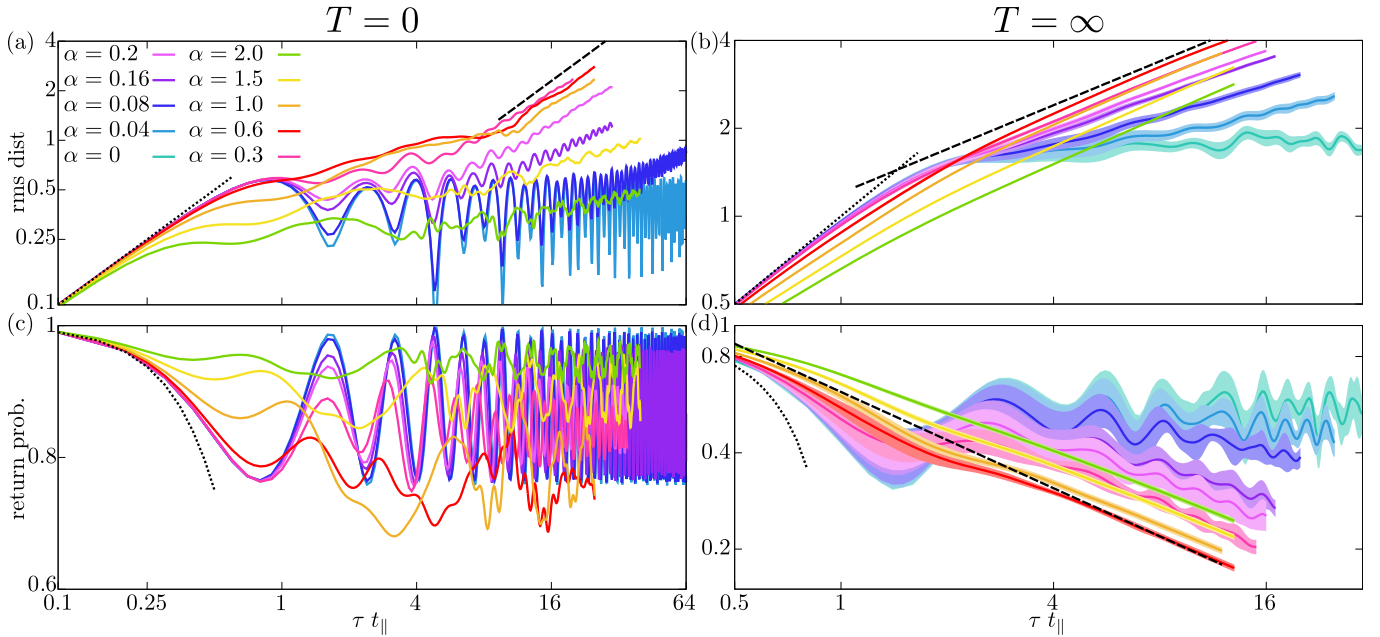


FIG. 4. **Dopant dynamics versus spin-exchange.** Rms dynamics of the dopant at zero (a) and infinite (b) temperatures for indicated values of the spin anisotropy, α , and $J = 5t_{\parallel}$. (c),(d) Corresponding probability for the dopant to return to its origin, $n_h(\mathbf{i} = \mathbf{0}, \tau)$. Short-dashed lines show the initial ballistic behavior, where $d_{\text{rms}}(\tau) = \tau t_{\parallel}$. Long-dashed lines in (a) show the final ballistic regime consistent with the formation of magnetic polaron quasiparticles, whereas the long-dashed lines in (b),(d) show diffusive behavior. Shaded areas show the estimated standard errors on the mean from 100 spin samples. For the TEBD, we use a truncation error of 10^{-7} and system sizes of $N_x \times N_y = 15 \times 2, 21 \times 2$ at low and high α at $T = 0$, whereas $N_x \times N_y = 11 \times 2$ for $T = \infty$.

the behavior of the charge (the dopant) and the spins at infinite temperature.

The total spin- z conserving dynamics of only spins is naturally encoded in the two-time spin correlator $S(x, \tau) = \langle \hat{S}^z(x, \tau) \hat{S}^z(x_0, 0) \rangle$, with the operator $\hat{S}^z(x, \tau) = \exp(i\hat{H}_J\tau) \hat{S}^z(x, 0) \exp(-i\hat{H}_J\tau)$ in the Heisenberg picture and $\hat{S}^z(x, 0) = \sum_{y=0,1} \hat{S}^z((x, y), 0)$ the sum of spin operators on rung x over both legs. Here, the origin rung x_0 is placed in the middle of the ladder rather than at the left edge. The corresponding rms distance of the spin dynamics is then given by

$$d_{\text{rms}}^s(\tau) = \left[\sum_x (x - x_0)^2 S^z(x, \tau) \right]^{1/2}, \quad (10)$$

so that the $[d_{\text{rms}}^s]^2$ is the width of a spreading wave packet of spin placed on the origin rung amidst a random spin background. To compute the spin correlator, we use the density matrix truncation algorithm, a modified MPS time evolution method designed to efficiently capture local properties of time-evolved density matrices [69]. We use a recently introduced variant for Heisenberg evolving operators beyond one dimension, such as our two-leg ladder system, with a 1D MPS ansatz. This algorithm enables us to go to considerably larger system sizes (501×2) and timescales ($Jt \sim 1600$) for the spin dynamics than for hole dynamics, which we find to be crucial to get accurate results [70], as we also comment further on below. The resulting rms dynamics are shown in Fig. 5(a) for

indicated values of the spin anisotropy. We are, hereby, in a position to directly compare the observed power-law behaviors in the rms distances

$$\begin{aligned} d_{\text{rms}}^h(\tau) &\rightarrow \sqrt{2D_h} \times (t_{\parallel}\tau)^{1/z_h}, \\ d_{\text{rms}}^s(\tau) &\rightarrow \sqrt{2D_s} \times (J\tau)^{1/z_s}, \end{aligned} \quad (11)$$

for the hole (top) and spin (bottom) degree of freedom. The inverse of the resulting dynamical exponents, $1/z_h, 1/z_s$ are shown in Fig. 5(b). Surprisingly, while one would naïvely expect a diffusive behavior for all nonzero spin anisotropies [71], we instead see that at sufficiently weak spin-exchange, $\alpha \ll 1$, the inverse dynamical exponent starts to significantly decrease, yielding *sub-diffusive* behavior, at least on the timescales reachable in numerics. This is most striking for the dopant, for which we find good agreement with the logarithmic behavior

$$\frac{1}{z_h(\alpha)} = c_1 \ln(\alpha) + c_2 \quad (12)$$

in the range $0.02 < \alpha < 0.3$. For even smaller α , this behavior eventually will break down, as $\ln(\alpha)$ diverges to $-\infty$ for $\alpha \rightarrow 0$. Instead, we expect a smooth, though very rapid, approach of $1/z(\alpha) \rightarrow 0$ for $\alpha \rightarrow 0$. The inverse of the spin dynamical exponent, $1/z_s$, has a much slower drop-off but eventually decreases as well. For both spins and holes, the expected diffusive behavior ($z_h = z_s = 2$) eventually appears for $\alpha \gtrsim 0.3$.

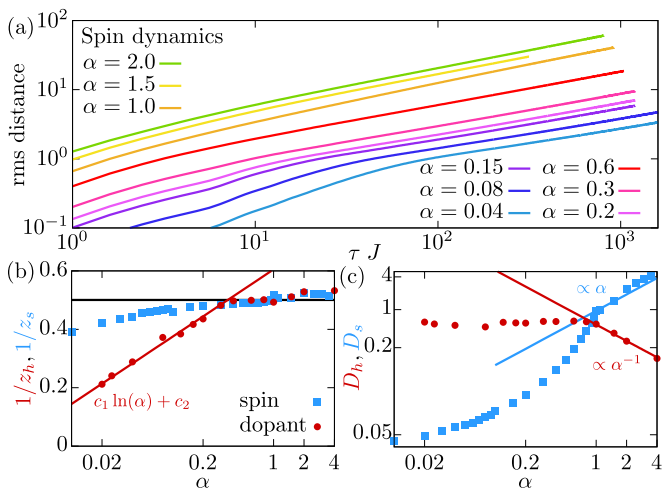


FIG. 5. **Spin versus charge dynamics.** (a) Rms spin dynamics at infinite temperature for indicated values of the spin anisotropy, α , in the absence of dopants. Note that time is now in units of the spin coupling, J . System sizes between 151×2 and 501×2 are used, and data end either at the maximal evolution time or when the boundary effects become non-negligible ($S(0, \tau)/S(x_0, \tau) > 10^{-3}$). (b) Fitted inverse dynamical exponent for the charge (red, $1/z_h$) and spin dynamics (blue, $1/z_s$) versus the spin anisotropy, α . The horizontal black line shows the diffusive exponent of $1/2$. (c) Corresponding diffusion coefficients, D_h, D_s . The blue line gives the expected linear scaling $D_s \propto \alpha$, while the red line shows α^{-1} scaling.

The most striking difference between the spin and charge degree of freedom, however, is seen by investigating the corresponding generalized diffusion coefficients D_h, D_s [Fig. 5(c)]. Whereas the coefficient for the hole, D_h , remains approximately constant for $\alpha < 1$, the spin coefficient drops off very rapidly as one approaches the Ising limit $\alpha \rightarrow 0$. Moreover, in the regime of large spin-exchange, $\alpha > 1$, the hole coefficient drops off as α^{-1} , while the spin coefficient *increases* linearly in α . The latter behavior is indeed expected from the well-studied XX model, which we approach for $\alpha \gg 1$. Here, previous studies have found $D_s \simeq 0.95\alpha$ [72–74], which is in good agreement with our results for $\alpha > 1$ [blue line in Fig. 5(c)]. In this manner, there is *qualitative* agreement between the behaviors of the spin and charge degrees of freedom. On the other hand, the dichotomy between the spins and the charge in their *quantitative* behavior shows that the charge is not simply diffusing with the underlying spins. This is especially evident from the behavior for $\alpha > 1$, where the spins diffuse faster, while the dopant diffuses slower. We also note that the (sub)-diffusive behavior for the dopant sets in already after a few hopping times $t_{\parallel}\tau \sim 5$ (or $J\tau \sim 25$) on very short length scales, the spin dynamics needs around $J\tau \sim 100$ and considerably larger length scales. This a posteriori justifies that we use only intermediate system sizes for the dopant dynamics, whereas we need much larger system sizes and timescales for the spin dynamics.

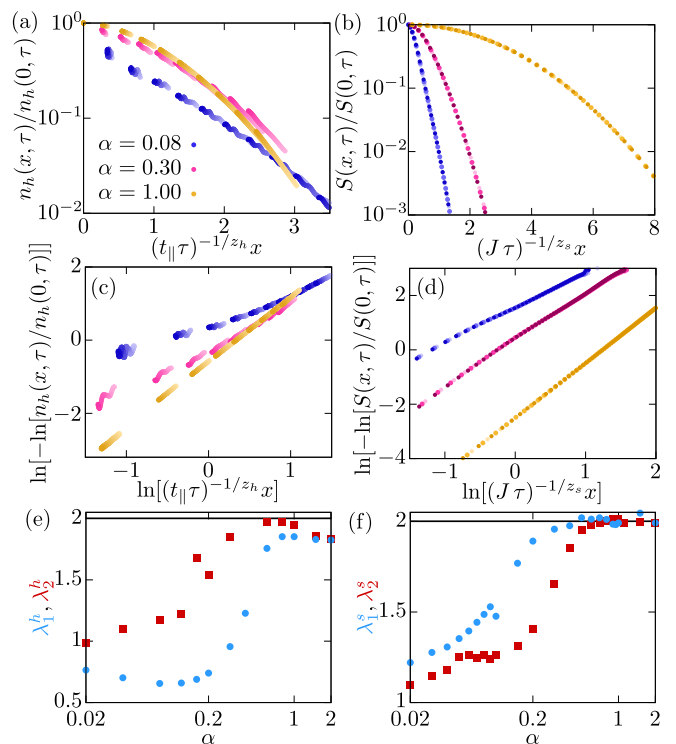


FIG. 6. **Self-similar scaling behavior.** Scaled hole distribution (a) and scaled spin-spin correlator (b) as a function of $\tau^{-1/z}x$ for indicated spin anisotropies α reveals a self-similar scaling behavior. The color gradient on the data points denote the evolution time from shortest used (bright colors) to longest used (dark colors). The used intervals are: (a) $t_{\parallel}\tau \in [12, 20], [10, 15], [8, 12]$ and (b) $J\tau \in [1400, 1600], [1000, 1200], [720, 920]$ for $\alpha = 0.08, 0.3, 1.0$. (c),(d) The double-logarithm of the scaled distribution versus $\ln[\tau^{-1/z}x]$ shows differing *linear* behaviors on short and long scales with slopes λ_1, λ_2 respectively. This describes generalized exponential distributions, $n_h \sim \exp[-(\tau^{-1/z_h}x)^{\lambda_h}]$, $S^z \sim \exp[-(\tau^{-1/z_s}x)^{\lambda_s}]$. The fitted general exponents λ_1, λ_2 at short and long scales for the hole distribution (e) and spin-spin correlator (f) are shown in blue and red, respectively, against the spin anisotropy, α . For low α , these *strongly* deviate from diffusive behavior (black lines: $\lambda = 2$).

To substantiate over findings about the sub-diffusive behavior, we demonstrate that the dynamics exhibit self-similar scaling behavior. While we cannot rule out that diffusion eventually sets in on sufficiently long timescales, this scaling behavior emphasizes that distinctly non-diffusive and non-Gaussian transport is robust in the limit of small spin exchanges. More concretely, Fig. 6(a) [Fig. 6(b)] shows the comparison between the rung hole distribution $n_h(x, \tau) = n_h(x, 0, \tau) + n_h(x, 1, \tau)$ and the rung spin correlator $S(x, \tau)$ for several values of the spin anisotropy, α . In Figs. 6(a) and 6(b), we use data from the sub-diffusive regime for the dopant and spin dynamics, respectively. Lengths are here rescaled by $\tau^{1/z}$, with the fitted dynamical exponents z_h, z_s in Fig. 5(b) for a range of times in the sub-diffusive regime. As a result of this rescaling, the data collapse onto a single

line for each value of α . This is a strong indicator that the dynamics takes on self-similar scaling behaviors at sufficiently long times,

$$\begin{aligned} n_h(x, \tau) &= \frac{1}{(t_{\parallel}\tau)^{1/z_h}} F_h \left(\frac{x}{(t_{\parallel}\tau)^{1/z_h}} \right), \\ S(x, \tau) &= \frac{1}{(J\tau)^{1/z_s}} F_s \left(\frac{x}{(J\tau)^{1/z_s}} \right), \end{aligned} \quad (13)$$

which is analogous to what one sees in standard diffusion arising from the diffusion equation, $\partial_{\tau} n = D \partial_x^2 n$. Indeed, in that case, subject to the initial condition $n(x, \tau = 0) = \delta(x)$, the scaling function $F(u)$ is simply a Gaussian [46]. One way to think of this self-similar behavior is that it defines the line along which the density (or spin correlator) at fixed position x flows as a function of time, as one may also see from the color gradient in Fig. 6(a). To test whether the distributions follow a similar pattern in our case, we replot them on a log double-log plot in Figs. 6(c) and 6(d). This reveals distinct linear behaviors at short and long scales. It follows that the scaling functions take on the limiting short- and long-range behaviors

$$F_i(u) \propto \begin{cases} \exp \left[- \left(\frac{u}{\sqrt{2}\sigma_1^i} \right)^{\lambda_1^i} \right], & u \lesssim 1, \\ \exp \left[- \left(\frac{u}{\sqrt{2}\sigma_2^i} \right)^{\lambda_2^i} \right], & u \gtrsim 1, \end{cases} \quad (14)$$

where $i = h, s$ indexes whether it is for the hole or spin degree of freedom. These generalized exponential functions, hereby, come with emergent exponents λ_1^i, λ_2^i on short and long scales, which we plot over a wide range of spin anisotropies in Figs. 6(e) and 6(f). For large enough α , these exponents are similar to one another and close to the regular Gaussian diffusive behavior of $\lambda = 2$. For lower α , however, they both start to deviate substantially from Gaussianity and each other. Interestingly, the charge and spin degree of freedom show opposite tendencies here. Whereas the hole distribution develops a cusp on short scales, with $\lambda_1^h < \lambda_2^h$, the spin distribution is soft at short scales and sharper at longer scales, $\lambda_1^s > \lambda_2^s$. Once again, this emphasizes the qualitative agreement between the spin and charge degrees of freedom, albeit with dichotomous quantitative behavior.

The strong deviation away from the Gaussian behavior at low α , which is otherwise inherent to diffusion, together with the strong suppression of the dynamical exponent in this regime, indicates that the system has settled into a pre-thermal self-similar scaling behavior [75–79]. Therefore, we believe that the discovered sub-diffusive dynamics is robust and persists to long timescales. It simultaneously suggests that it is very difficult to find an effective hydrodynamic description. Indeed, while *rescaled diffusion* [80] could in principle describe the *continuous* behavior of the dynamical exponent that we observe, this would still be described

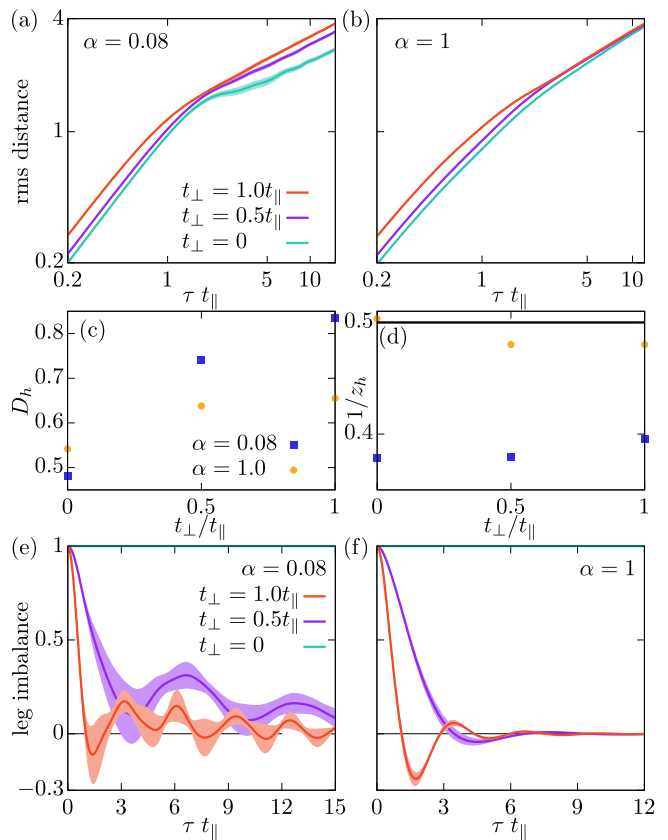


FIG. 7. **Rung hopping dependency.** (a),(b) Dopant rms dynamics at indicated spin anisotropies, α , and transverse hopping, t_{\perp} . While the associated diffusion coefficients (c) increases with t_{\perp} , the dynamical exponents (d) remains almost unaltered. (e),(f) The leg imbalance [Eq. (15)] shows that the legs of the ladder thermalize on a timescale depending on t_{\perp} and α . Shaded areas show the estimated standard error from 100 spin samples. We use a truncation error of 10^{-7} and $N_x \times N_y = 11 \times 2$.

by a Gaussian scaling function. On the other hand, scaling functions differing from Gaussian behavior has been observed in dipole-conserving spin models [78] well-described by hydrodynamics. However, in this case the effective hydrodynamic equation has a higher-order spatial derivative, $\partial_x^2 \rightarrow \partial_x^{(2m+1)}$ for integers m , which fixes the dynamical exponent to be an integer, $z = (2m + 1)$. In our case, there is, therefore, seemingly a simultaneous breaking of simple hydrodynamics and retained self-similar scaling behavior.

B. Rung hopping

To complete our understanding of the dynamical phase diagram in Fig. 1(d), we now investigate whether the discovered sub-diffusion is a result of the proximity to the *fragmented phase* at $\alpha = t_{\perp} = 0$. To investigate this, we track the hole motion at nonzero rung hoppings, $t_{\perp}/t_{\parallel} = 0.5, 1$, at spin anisotropies $\alpha = 0.08$ and 1.

The analysis shown in Fig. 7 reveals that the diffusive behavior at $\alpha = 1$ is robust to changes in the transverse hopping t_\perp and that the long-time behavior of $t_\perp = 0.5t_\parallel$ and $t_\perp = t_\parallel$ collapses on longer timescales. Moreover, for both values of α , the inverse dynamical exponent, $1/z$, in Fig. 7(d) is *insensitive* to $t_\perp > 0$, whereas the generalized diffusion coefficient, D_h , increases with t_\perp , as one might expect. In this manner, the sub-diffusive behavior appears to *not* be a special property only *close* to the fragmented phase at $\alpha = t_\perp = 0$ but holds much more generally in the proximity of the *localized phase* at $\alpha = 0$.

Finally, the presence of a nonzero t_\perp gives us a natural way of probing the thermalization of the system. In Figs. 7(e) and 7(f), we show the leg imbalance

$$\mathcal{I}(\tau) = \sum_x [n_h((x, 0), \tau) - n_h((x, 1), \tau)], \quad (15)$$

measuring the difference in hole density in the two legs of the ladder. When $t_\perp = 0$, the hole cannot hop to the other leg, whereby $I_l = 1$. For $t_\perp > 0$, however, we see that that the leg imbalance diminishes over time with heavily damped oscillations around $I_l = 0$, which indicates that the dopant eventually “forgets” that it was initially localized on the $y = 0$ leg, showing the anticipated thermalization. This process is, however, significantly slower for small spin anisotropies. We note that in the extreme Ising limit of $\alpha = 0$, I_l remains nonzero on all timescales, evidencing the localization-induced lack of thermalization described in Sec. IV.

C. Temperature dependency

Let us now address how the system crosses over from its (sub)-diffusive behavior at infinite temperature to ballistic behavior at zero temperature. To this end, and as explained in Sec. III, we use METTS to sample the thermal background of the spins. The exact methodology is detailed in App. C, where we also show that the achieved ensembles show no discernible autocorrelations. The resulting rms dynamics are shown in Fig. 8 for indicated values of the spin anisotropy and $t_\perp = 0$. We note that at a fixed time, the rms distance smoothly crosses over from its infinite to zero temperature value. Moreover, at high temperatures $\beta J = J/k_B T \leq 2$, we find that the generalized diffusion coefficient D_h at fixed J/t_\parallel is very well described by an Arrhenius relation

$$D_h(\alpha, \beta J) = D_h(\alpha, 0) \exp[-\varepsilon(\alpha)\beta J], \quad (16)$$

in which $D_h(\alpha, 0)$ is the infinite temperature diffusion coefficient. In this manner, D_h decreases *exponentially* with decreasing temperatures, as evident from the insets in Fig. 8. Arrhenius originally suggested this relation for molecular reaction rates at high temperatures [47]. It is also gives an accurate description of impurity diffusivity in the bulk [81–83] and on the surface of

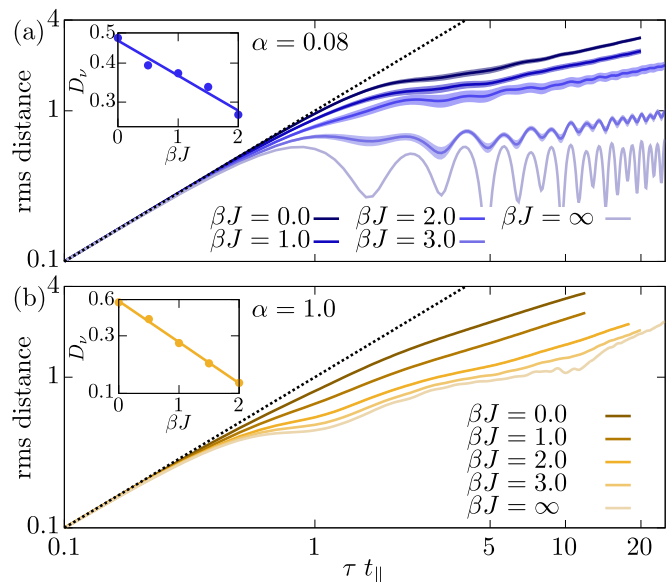


FIG. 8. **Temperature dependency of sub-diffusion.** Rms dynamics for indicated inverse temperatures, βJ , and spin anisotropies $\alpha = 0.08$ (a), $\alpha = 1$ (b), at $J = 5t_\parallel$ and $t_\perp = 0$. Dashed lines: initial ballistic behavior. Insets: extracted diffusion coefficients as a function of inverse temperature on a linear-log scale, where colored lines show fits to the Arrhenius form in Eq. (16). Shaded areas show the estimated standard error from 100 METTS samples. For the TEBD, we use a truncation error of 10^{-7} and $N_x \times N_y = 13 \times 2$.

metals [84] at high temperatures and may even be derived from rather general classical statistical-mechanical considerations [85]. It is, however, to the best of our knowledge, the first time that such a relation emerges from a first-principle quantum-mechanical description. The Arrhenius form also suggests that we can interpret ε as an *activation energy* of the diffusive process. We note that the activation energy is considerably lower for $\alpha = 0.08$ [Fig. 8(a)] than for $\alpha = 1$ [Fig. 8(b)]. Qualitatively, we can understand this behavior from the fact that the *change in magnetic energy* in a single hopping event fluctuates more for larger α . Indeed, for infinite temperatures this can be evaluated to yield fluctuations with a standard deviation of $\text{std}(\Delta E_J) = J [1 + 2\alpha^2]^{1/2} / 2$, which indeed increases with α [see App. D for details]. This simple expression, however, underestimates the ratio of $\varepsilon(\alpha = 1)/\varepsilon(\alpha = 0.08) = 3.0 \pm 0.2$ fitted from the insets of Fig. 8 by a factor of ~ 0.6 . This discrepancy is presumably due to the fact that one should rather describe the process not at short distance scales but for minute long-wavelength corrections to the thermal background.

The mere appearance of an Arrhenius relation indicates that we can think of the diffusion process semi-classically in the following way. When the dopant moves, it must cross an energy barrier given by the magnetic fluctuations. At infinite temperature, the dopant completely disregards this barrier and moves with a diffusion coefficient $D_h(\alpha, \beta J = 0)$. As the temperature is low-

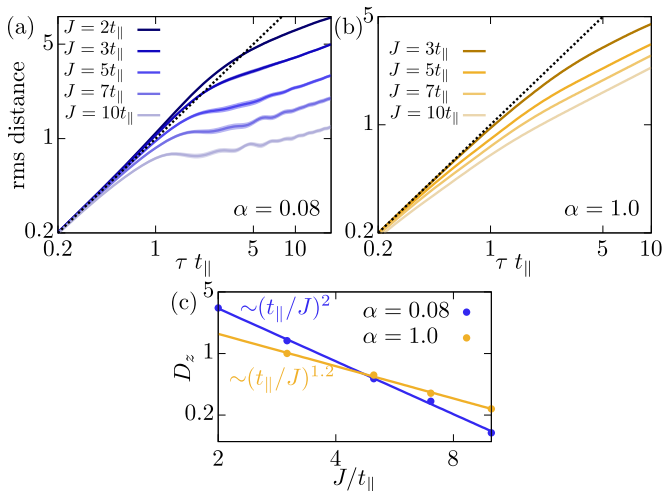


FIG. 9. Spin coupling dependency of sub-diffusion. Dopant rms dynamics for indicated values of the spin coupling, J , deep in the sub-diffusive regime (a) and deep in the diffusive regime (b), both for $t_{\perp} = 0$. In both cases, the dynamical exponent is minimally affected, whereas the generalized diffusion coefficients (c) depend sensitively on J/t_{\parallel} and is well-described by the indicated power-laws (lines). Shaded areas show the estimated standard error from 100 samples. For the TEBD, we use a truncation error of 10^{-7} . For $\alpha = 1$, $N_x \times N_y = 13 \times 2$, whereas for $\alpha = 0.08$ it ranges from $N_x \times N_y = 13 \times 2$ at $J = 10t_{\parallel}$ to $N_x \times N_y = 31 \times 2$ at $J = 2t_{\parallel}$ to capture the faster increase in the rms dynamics as J/t_{\parallel} is lowered.

ered, however, it becomes increasingly difficult for the dopant to cross the barrier leading to the exponential reduction in Eq. (16). We believe that this should hold whenever the spin couplings dominate the hopping process, $J/t \gg 1$. At intermediate and low values of J/t , this simple picture could break down. However, this regime is technically challenging to access, because the dopant in this case has a prolonged initial ballistic regime, and so we would need to do computations for increasingly large spin lattices.

We note that at sufficiently low temperatures, we expect a strong deviation from this behavior. Indeed, this regime should eventually be described by transient ballistic quasiparticle behavior, which in turn should lead to a diverging diffusion coefficient at low enough temperatures, though we have not been able to push our MPS calculations to resolve such a ballistic to diffusive crossover. Consequently, at sufficiently long times the zero temperature ($\beta J = \infty$) ballistic curve must eventually cross all the rms distance curves for nonzero temperatures ($\beta J < \infty$). One also sees the first indications of these crossings in Fig. 8(b) between the $\beta J = 3$ and $\beta J = \infty$ results.

D. Spin coupling dependency

In this subsection, we investigate quantitatively the dependency of the (sub)-diffusion on the ratio between the

spin coupling and the hopping amplitude, J/t_{\parallel} , at infinite spin temperatures. The resulting dopant rms dynamics are shown in Fig. 9(a)-(b). We find that the dynamical exponent only changes very little over the investigated range of J/t_{\parallel} . Indeed, the lines in Fig. 9(a)-(b) are almost perfectly parallel at long times. This shows that the sub-diffusive behavior is not particular to the regime of very high spin couplings of $J \sim 5t_{\parallel}$ investigated so far, but holds up very well at lower spin couplings down to at least $J/t_{\parallel} = 2$. It becomes increasingly difficult, however, to carry out MPS calculations at lower J/t_{\parallel} for the simple reason that the dopant delocalizes faster, such that larger system sizes are needed to alleviate finite-size effects. In the investigated regime, we further see that the generalized diffusion coefficient exhibits a power-law decrease in t_{\parallel}/J [Fig. 9(c)]

$$D_h \propto \left(\frac{t_{\parallel}}{J}\right)^{\gamma(\alpha)}. \quad (17)$$

For weak spin-exchange, i.e. $\alpha = 0.08$, the data is in excellent agreement with a perturbative scaling of $\gamma(\alpha = 0.08) = 2$. We expect this to hold in general for $\alpha \ll 1$. On the other hand, the behavior at the isotropic point is greatly altered to a much slower power-law drop of merely $\gamma(\alpha = 1) \simeq 1.2$.

VI. TOWARDS TWO-DIMENSIONAL LATTICES

In this section, we discuss how our results may generalize to a fully two-dimensional system. We start in the Ising limit, $\alpha = 0$ with isotropic hopping amplitudes $t_{\perp} = t_{\parallel} \equiv t$, for which we can make precise qualitative arguments. In this case, we hypothesize that the dopant is still localized at high temperatures, $\beta J \rightarrow 0$, and that this remains true even across the Ising phase transition at $\beta_c J = 2 \ln[1 + 2^{-1/2}] \simeq 1.76$ [86]. To see why, we compute the magnetic energy landscape seen by the dopant as it travels through the Ising magnet, i.e. $E_J(\boldsymbol{\sigma}, l) = \langle \psi_{\boldsymbol{\sigma}}(l) | \hat{H}_J | \psi_{\boldsymbol{\sigma}}(l) \rangle - \langle \psi_{\boldsymbol{\sigma}}(0) | \hat{H}_J | \psi_{\boldsymbol{\sigma}}(0) \rangle$ in complete analogy with Fig. 2(h). In 2D, it may not be enough that this landscape is disordered to ensure dopant localization, since 2D is the lower critical dimension for Anderson localization [87]. This is in contrast to Anderson localization in one dimension [51, 88], as well as our present findings for the two-leg ladder in the Ising limit [see Fig. 2]. However, if this landscape inevitably fluctuates more and more as a function of traveled distance of the dopant, this is a very strong argument for localization. In fact, if the magnetic energy at a traveled distance of l has a standard deviation $\text{std}[E_J(\boldsymbol{\sigma}, l)] = J \times (l/l_{\text{fl}})^a$ for some power $a > 0$, the dopant should *only* be able to travel out to distances where the fluctuations surpass its initial kinetic energy. This distance is set by $t \sim \text{std}[E_J(\boldsymbol{\sigma}, l)]$, leading to a localization length on the order of $l_{\text{loc}} \sim l_{\text{fl}}(t/J)^{1/a}$ [2].

To be more explicit, in the Ising limit where we can analyze classical spin configurations with one spin removed, we use classical Monte-Carlo sampling of the spin background [2, 66, 89] to produce 2000 samples of size $N_x \times N_y = 201 \times 201$ for a range of inverse temperatures and initialize the hole (the dopant) at the central site of the lattice. At low temperatures, the eventual delocalization of the dopant is enabled by Trugman loops [90] as discussed in Sec. IV and shown in Fig. 2(a). In a single Trugman loop, the dopant travels along one of the four diagonals $(x, y) \rightarrow (x \pm 1, y \pm 1)$. Thus we can check how small the magnetic energy changes experienced by the dopant can possibly be by the following iterative process. At each site, we compute the *change* in energy following one of the four Trugman loops. We then pick the site with the lowest energy change as the next starting point, update the spin background accordingly and repeat the procedure. To ensure that the dopant does not get stuck, we do *not* allow it to retrace its own path. This will generate a path with the smallest possible change in magnetic energy from a local update rule and leads, in particular instances, to the paths shown in Figs. 10(a) and 10(b). We note that in Fig. 10(b), the system is below the critical temperature, $\beta > \beta_c$ and has spontaneously chosen the configuration with a majority of antiferromagnetic domains with staggered magnetization $M(x, y) = (-1)^{x+y} S^z(x, y) = -1/2$ (blue regions).

In this manner, the dopant travels more easily in the antiferromagnetic ($\beta > \beta_c$) phase than in the paramagnetic ($\beta < \beta_c$) phase. Indeed, in Figs. 10(c)-(d), we show the corresponding change in magnetic energy, $E_J(\sigma, l)$, as a function of traveled distance l for 100 of the 2000 samples, σ . We see that at infinite temperatures [Fig. 10(c)], this is symmetric around $E_J = 0$, whereas it becomes asymmetric and has much smaller fluctuations in the antiferromagnetic phase [Fig. 10(d)]. Moreover, we numerically find that the standard deviation of the magnetic energy,

$$\text{std}[E_J(l)]^2 = \frac{1}{|S|} \sum_{s \in S} E_J^2(s, l) - \left(\frac{1}{|S|} \sum_{s \in S} E_J(s, l) \right)^2, \quad (18)$$

calculated from the Monte-Carlo generated set S of $|S| = 2000$ spin samples, retains a power-law behavior, $\text{std}[E_J(l)] = J \times (l/l_{\text{fl}})^{\alpha}$, across the phase transition [Fig. 10(e)]. This is similar to the $l^{1/2}$ behavior described in Fig. 2(g) for $t_{\perp} = 0$, and simultaneously shows that the bounded behavior of $\text{std}[E_J(l)]$ for $t_{\perp} > 0$ [Fig. 2(g)] is particular to the two-leg ladder. This behavior strongly suggests that the dopant is localized at infinite temperatures and that this *remains true* across the phase transition, though with a larger localization length. In this manner, the associated fluctuation length scale l_{fl} , with which the localization length should scale, is finite across the phase transition [Fig. 10(f)] and only shows a mild increase just around the critical temperature. At slightly lower temperatures (larger β), it does, however, increase much more rapidly than in the case of 1D motion ($t_{\perp} = 0$) of a dopant in a 2D Ising magnet [2]. Indeed, the increase

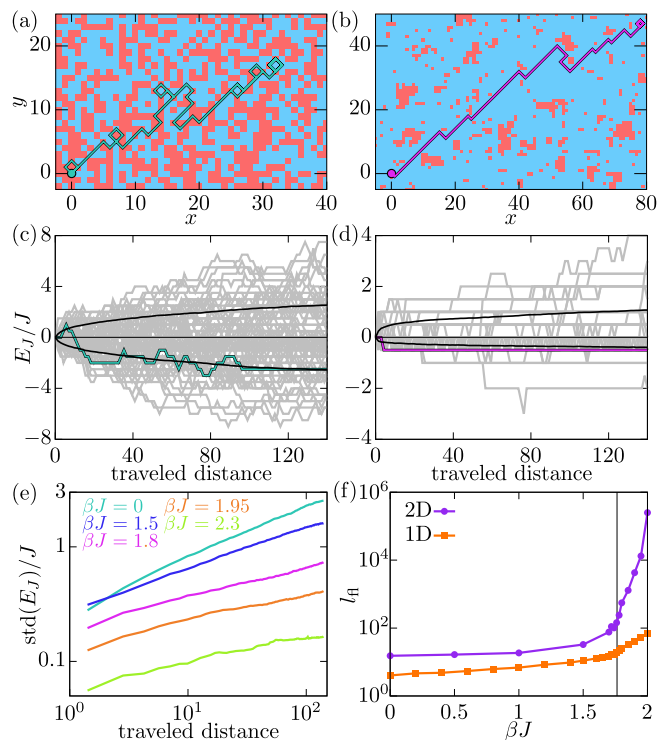


FIG. 10. **2D motion in an Ising magnet.** Low-energy trajectories (colored lines) of a dopant in the paramagnetic phase at $\beta J = 0$ (a), and in the antiferromagnetic phase at $\beta J = 1.8$ (b) shown for a specific Monte-Carlo sample of the spin background. The staggered spin pattern of this sample, $M(x, y) = (-1)^{x+y} S^z(x, y)$, is shown in the background in red [$M = +1/2$] and blue [$M = -1/2$]. (c),(d) Magnetic energy versus traveled distance by the dopant is shown for the same inverse temperatures [(c): $\beta J = 0$, (d): $\beta J = 1.8$] for 100 Monte-Carlo samples of the background [gray lines] and the particular ones used in (a),(b) [colored lines]. Black lines show the mean of E_J plus/minus one standard deviation, $\mu(E_J) \pm \text{std}(E_J)$, computed from 2000 spin samples. (e) Standard deviation $\text{std}(E_J)$ versus traveled distance of the dopant for indicated inverse temperatures. (f) Corresponding fluctuation length scale from power-law fit, $\text{std}[E_J(l)]/J = (l/l_{\text{fl}})^{\alpha}$, for 2D (purple dots) and 1D (orange squares) motion of the dopant.

in $\text{std}[E_J(l)]$ at the lowest investigated temperatures of $\beta J = 2.3$ versus traveled distance l becomes very slow and perhaps even levels off at large distances. Taken together, this indicates that the localization length remains finite across the phase transition, but becomes parametrically large as the temperature is decreased. Finally, since the fluctuation length scale l_{fl} seemingly increases exponentially below the phase transition, we can expect quasiparticles with correspondingly long lifetimes on the order of the time it takes them to travel to the localization length, $\sim l_{\text{fl}}/v_q$, where v_q is a typical quasiparticle propagation speed.

A distinct possibility, however, is that below the phase transition, the dopant behaves as a charge scattering on static point-like impurities. This scenario naturally

arises in impure metallic conductors and in 2D gives rise to weak localization [91–94], in which the resistivity increases logarithmically at low temperatures. Indeed, one might think of the small $M = +1/2$ domains in Fig. 10 as such static point-like impurities that the dopant is scattering off. Following this logic, the impurity density decreases with decreasing temperatures as the system becomes more antiferromagnetically ordered. If this is the correct physical picture, the dopant should go from being localized above the critical temperature to diffusing below the critical temperature. Moreover, as temperature decreases to zero long-lived quasiparticles should also emerge in this scenario, whereby the diffusion coefficient diverges in this limit, and dopants may finally move ballistically.

Finally, in the presence of spin-exchange processes we have no reason to believe that the high-temperature behavior should change qualitatively as we go to two dimensions. Indeed, as a first small step towards the full 2D behavior, we saw that the inclusion of transversal hopping, $t_{\perp} > 0$, had no *qualitative* impact on the motion. Moreover, it seems that exactly the same processes will be available both in the ladder and in the full 2D case. We, therefore, strongly believe that this will remain true even as more legs of the ladder are added and even in the true 2D limit. One plausible scenario, however, is that the parameter regime supporting sub-diffusive motion decreases as more legs of the ladder are added and that eventually only the diffusive regime for any nonzero spin-exchange, $\alpha > 0$, remains.

We note, however, that this extension of our results is seemingly in contradiction with recent results for a four-leg ladder in the isotropic Heisenberg limit ($\alpha = 1$) [95], in which a curious sub-diffusive $\tau^{1/4}$ behavior is found at long times, instead of the more standard $\tau^{1/2}$ diffusive behavior that we presently find for $\alpha = 1$. While we presently do not know how to resolve this seeming discrepancy, we note that their MPS methodology is different from ours [96]. While we utilize a combination of METTS with TDVP and use TEBD for real-time evolution, they use a purification scheme [97] along with TDVP for real-time evolution [60, 61]. In our studies, we have seen that we *can* reproduce our TEBD results with TDVP but it requires that we take very special care of how the subspace expansion method [59] is implemented. Additionally, we note that diffusive transport in the infinite temperature 2D Heisenberg model ($\alpha = 1$) has been observed both experimentally in a cold atom quantum gas microscope experiment [17] and numerically in simulations on cylinders of width up to 8 [70]. The spin dynamics do not necessarily dictate the dopant dynamics, but at least in the case of the two-leg ladder studied here, we find qualitative agreement between them, in particular the diffusion in the Heisenberg limit (see Fig. 5).

VII. CONCLUSIONS

Using MPS calculations, we have thoroughly investigated the transport of a single charge (a hole) moving via nearest-neighbor hopping, t , in an XXZ spin ladder. We demonstrated that the charge is localized in the Ising limit, i.e. in the absence of spin-exchange processes, at all investigated nonzero temperatures and that the accompanying localization length scales with the underlying spin-spin correlation length. This greatly generalizes the results of the previously studied Hilbert space fragmented models [1, 2].

We have shown that spin-exchange processes $\propto \alpha$ lead to delocalization of charge and spin degrees of freedom alike according to a power-law behavior in time, $\tau^{1/z}$, that *smoothly interpolates* between localization ($1/z = 0$) at $\alpha = 0$ and diffusion ($1/z = 1/2$) for $\alpha \gtrsim 0.3$, giving a range of sub-diffusive behavior for $0 < \alpha \lesssim 0.3$. The charge and spin distributions are, furthermore, demonstrated to follow self-similar scaling behaviors that in the sub-diffusive regime strongly deviate from the Gaussian behavior of regular diffusion. This suggests a simultaneous breakdown of simple hydrodynamics [71, 98] but with retained pre-thermal self-similar scaling.

Moreover, we have shown robust sub-diffusion over a wide range of high temperatures ($J/k_B T \lesssim 2$) and spin couplings ($J \gtrsim 2t$). Finally, we conjecture that these findings generalize to fully two-dimensional spin lattices. In particular, in the Ising limit we anticipate that the charge will undergo a very fast delocalization *crossover* as the para- to antiferromagnetic transition is crossed. Moreover, we believe that the observed sub-diffusive behavior is not dependent on the ladder structure and will remain in two dimensions.

Our findings show that Hilbert space fragmentation [9, 10] in the present case is not a necessary condition to ensure localization, nor does the proximity to such a fragmented model necessarily lead to special behavior. Instead, we posit that it is the much more general appearance of an effective disordered potential in the Ising limit (in complete analogy to Anderson localization [51]), which holds the key to the localization effect, whereas sub-diffusion appears in the *proximity* of this localized phase. This exemplifies that while Hilbert space fragmentation is a valuable computational property for investigating novel non-equilibrium quantum many-body dynamics, the origin of the discovered effects in such a regime is not necessarily due to the fragmentation itself.

In the future, we hope to explore how our present findings impacts the recently discovered spin disorder-induced pairing mechanism [48] in the fragmented phase. Indeed, when spin-exchange is weak, $\alpha J \ll t_{\parallel}$, we expect dopant pairing to be retained, because the internal dynamics of the pair $\sim t_{\parallel}$ is fast compared to the spin dynamics of the environment $\sim \alpha J$. For strong enough spin-exchange, the dopants might unbind and give rise to non-trivial dependencies on the spin coupling.

ACKNOWLEDGMENTS

The authors thank Steven R. White, J. Ignacio Cirac, Sarang Gopalakrishnan, Pavel Kos, and Jens H. Nyhgen for stimulating discussions and important input. The numerical calculations are performed using the ITensor library in Julia [99] and the TeNPy library in Python [100, 101]. K.K.N. acknowledges support from the Carlsberg Foundation through a Carlsberg Reintegration Fellowship (Grant No. CF24-1214). S.A. is supported by the U.S. Department of Energy, Office of Science, Of-

fice of Basic Energy Sciences, Materials Sciences and Engineering Division under Contract No. DE-AC02-05-CH11231 (Theory of Materials program KC2301). Part of this research uses the Lawrence Livermore computational cluster provided by the Lawrence Berkeley National Laboratory (supported by the U.S. Department of Energy, Office of Basic Energy Sciences under Contract No. DE-AC02-05-CH11231). M.Y. is supported by the Distinguished Postdoc Fellowship of the Munich Center for Quantum Science and Technology (MCQST) funded by DFG under the Excellence Strategy EXC2111-390814868.

-
- [1] K. K. Nielsen, Phys. Rev. Res. **6**, 023325 (2024).
 [2] K. K. Nielsen, SciPost Phys. Core **7**, 054 (2024).
 [3] M. B. Hastings, Journal of Statistical Mechanics: Theory and Experiment **2007**, P08024 (2007).
 [4] J. Eisert, M. Cramer, and M. B. Plenio, Rev. Mod. Phys. **82**, 277 (2010).
 [5] S. R. White, Phys. Rev. Lett. **69**, 2863 (1992).
 [6] P. Jurcevic, H. Shen, P. Hauke, C. Maier, T. Brydges, C. Hempel, B. P. Lanyon, M. Heyl, R. Blatt, and C. F. Roos, Phys. Rev. Lett. **119**, 080501 (2017).
 [7] S. Karch, S. Bandyopadhyay, Z.-H. Sun, A. Impertro, S. Huh, I. P. Rodríguez, J. F. Wienand, W. Ketterle, M. Heyl, A. Polkovnikov, I. Bloch, and M. Aidelsburger, Probing quantum many-body dynamics using subsystem loschmidt echos (2025), arXiv:2501.16995 [cond-mat.quant-gas].
 [8] H. Bernien, S. Schwartz, A. Keesling, H. Levine, A. Omran, H. Pichler, S. Choi, A. S. Zibrov, M. Endres, M. Greiner, V. Vuletić, and M. D. Lukin, Nature **551**, 579 (2017).
 [9] S. Moudgalya, B. A. Bernevig, and N. Regnault, Reports on Progress in Physics **85**, 086501 (2022).
 [10] S. Moudgalya and O. I. Motrunich, Phys. Rev. X **12**, 011050 (2022).
 [11] D. Adler, D. Wei, M. Will, K. Srakaew, S. Agrawal, P. Weckesser, R. Moessner, F. Pollmann, I. Bloch, and J. Zeiher, Nature **636**, 80 (2024).
 [12] W. S. Bakr, J. I. Gillen, A. Peng, S. Fölling, and M. Greiner, Nature **462**, 74 (2009).
 [13] J. F. Sherson, C. Weitenberg, M. Endres, M. Cheneau, I. Bloch, and S. Kuhr, Nature **467**, 68 (2010).
 [14] L. W. Cheuk, M. A. Nichols, M. Okan, T. Gersdorf, V. V. Ramasesh, W. S. Bakr, T. Lompe, and M. W. Zwierlein, Phys. Rev. Lett. **114**, 193001 (2015).
 [15] E. Haller, J. Hudson, A. Kelly, D. A. Cotta, B. Peaudecerf, G. D. Bruce, and S. Kuhr, Nature Physics **11**, 738 (2015).
 [16] C. Gross and W. S. Bakr, Nature Physics **17**, 1316 (2021).
 [17] D. Wei, A. Rubio-Abadal, B. Ye, F. Machado, J. Kemp, K. Srakaew, S. Hollerith, J. Rui, S. Gopalakrishnan, N. Y. Yao, I. Bloch, and J. Zeiher, Science **376**, 716–720 (2022).
 [18] C. Gross and I. Bloch, Science **357**, 995 (2017).
 [19] L. Tarruell and L. Sanchez-Palencia, Comptes Rendus. Physique **19**, 365 (2018).
 [20] F. Schäfer, T. Fukuhara, S. Sugawa, Y. Takasu, and Y. Takahashi, Nature Reviews Physics **2**, 411 (2020).
 [21] D. Greif, T. Uehlinger, G. Jotzu, L. Tarruell, and T. Esslinger, Science **340**, 1307 (2013).
 [22] R. A. Hart, P. M. Duarte, T.-L. Yang, X. Liu, T. Paiva, E. Khatami, R. T. Scalettar, N. Trivedi, D. A. Huse, and R. G. Hulet, Nature **519**, 211 (2015).
 [23] M. Boll, T. A. Hilker, G. Salomon, A. Omran, J. Nespolo, L. Pollet, I. Bloch, and C. Gross, Science **353**, 1257 (2016).
 [24] M. F. Parsons, A. Mazurenko, C. S. Chiu, G. Ji, D. Greif, and M. Greiner, Science **353**, 1253 (2016).
 [25] L. W. Cheuk, M. A. Nichols, K. R. Lawrence, M. Okan, H. Zhang, E. Khatami, N. Trivedi, T. Paiva, M. Rigol, and M. W. Zwierlein, Science **353**, 1260 (2016).
 [26] A. Mazurenko, C. S. Chiu, G. Ji, M. F. Parsons, M. Kanász-Nagy, R. Schmidt, F. Grusdt, E. Demler, D. Greif, and M. Greiner, Nature **545**, 462 (2017).
 [27] D. Mitra, P. T. Brown, E. Guardado-Sanchez, S. S. Kondov, T. Devakul, D. A. Huse, P. Schauß, and W. S. Bakr, Nature Physics **14**, 173 (2018).
 [28] T. Hartke, B. Oreg, C. Turnbaugh, N. Jia, and M. Zwierlein, Science **381**, 82 (2023).
 [29] J. R. Schrieffer and J. S. Brooks, *Handbook of high-temperature superconductivity* (Springer, 2007).
 [30] J. Koepsell, J. Vijayan, P. Sompet, F. Grusdt, T. A. Hilker, E. Demler, G. Salomon, I. Bloch, and C. Gross, Nature **572**, 358 (2019).
 [31] T. Chalopin, P. Bojović, S. Wang, T. Franz, A. Sinha, Z. Wang, D. Bourgund, J. Obermeyer, F. Grusdt, A. Bohrdt, L. Pollet, A. Wietek, A. Georges, T. Hilker, and I. Bloch, Probing the magnetic origin of the pseudogap using a fermi-hubbard quantum simulator (2024), arXiv:2412.17801 [cond-mat.str-el].
 [32] G. Ji, M. Xu, L. H. Kendrick, C. S. Chiu, J. C. Brüggenjürgen, D. Greif, A. Bohrdt, F. Grusdt, E. Demler, M. Lebrat, and M. Greiner, Phys. Rev. X **11**, 021022 (2021).
 [33] S. Schmitt-Rink, C. M. Varma, and A. E. Ruckenstein, Phys. Rev. Lett. **60**, 2793 (1988).
 [34] C. L. Kane, P. A. Lee, and N. Read, Phys. Rev. B **39**, 6880 (1989).
 [35] K. K. Nielsen, T. Pohl, and G. M. Bruun, Phys. Rev. Lett. **129**, 246601 (2022).
 [36] K. K. Nielsen, M. Zwierlein, and G. M. Bruun, Dual spectroscopy of quantum simulated fermi-hubbard systems (2025), arXiv:2503.03477 [cond-mat.quant-gas].
 [37] D. N. Sheng, Y. C. Chen, and Z. Y. Weng, Phys. Rev.

- Lett. **77**, 5102 (1996).
- [38] K. Wu, Z. Y. Weng, and J. Zaanen, Phys. Rev. B **77**, 155102 (2008).
- [39] Z. Zhu and Z.-Y. Weng, Phys. Rev. B **92**, 235156 (2015).
- [40] S. R. White, D. J. Scalapino, and S. A. Kivelson, Phys. Rev. Lett. **115**, 056401 (2015).
- [41] R.-Y. Sun, Z. Zhu, and Z.-Y. Weng, Phys. Rev. Lett. **123**, 016601 (2019).
- [42] J.-Y. Zhao, S. A. Chen, H.-K. Zhang, and Z.-Y. Weng, Phys. Rev. X **12**, 011062 (2022).
- [43] A. Bohrdt, F. Grusdt, and M. Knap, New Journal of Physics **22**, 123023 (2020).
- [44] J. Carlström, N. Prokof'ev, and B. Svistunov, Phys. Rev. Lett. **116**, 247202 (2016).
- [45] M. Kanász-Nagy, I. Lovas, F. Grusdt, D. Greif, M. Greiner, and E. A. Demler, Phys. Rev. B **96**, 014303 (2017).
- [46] J. Crank, Methods of solution when the diffusion coefficient is constant, in *The Mathematics of Diffusion* (Oxford University Press, 1975) p. 11–13.
- [47] S. Arrhenius, Zeitschrift für Physikalische Chemie **4U**, 96 (1889).
- [48] K. K. Nielsen, Phys. Rev. Res. **7**, L012033 (2025).
- [49] A. Smith, J. Knolle, D. L. Kovrizhin, and R. Moessner, Phys. Rev. Lett. **118**, 266601 (2017).
- [50] G. Gyawali, S. Kumar, Y. D. Lensky, E. Rosenberg, A. Szasz, T. Cochran, R. Chen, A. H. Karamlou, K. Kechedzhi, J. Berndtsson, T. Westerhout, A. Afaw, D. Abanin, R. Acharya, L. A. Beni, *et al.*, Observation of disorder-free localization using a (2+1)d lattice gauge theory on a quantum processor (2025), arXiv:2410.06557 [quant-ph].
- [51] P. W. Anderson, Phys. Rev. **109**, 1492 (1958).
- [52] In disorder-free localization, the local gauge symmetries commute and are responsible for the Hilbert space fragmentation.
- [53] J. Zeiher, J.-y. Choi, A. Rubio-Abadal, T. Pohl, R. van Bijnen, I. Bloch, and C. Gross, Phys. Rev. X **7**, 041063 (2017).
- [54] P. Weckesser, K. Srakaew, T. Blatz, D. Wei, D. Adler, S. Agrawal, A. Bohrdt, I. Bloch, and J. Zeiher, Realization of a rydberg-dressed extended bose hubbard model (2024), arXiv:2405.20128 [cond-mat.quant-gas].
- [55] L. Homeier, T. J. Harris, T. Blatz, S. Geier, S. Hollerith, U. Schollwöck, F. Grusdt, and A. Bohrdt, Phys. Rev. Lett. **132**, 230401 (2024).
- [56] M. Qiao, G. Emperauger, C. Chen, L. Homeier, S. Hollerith, G. Bornet, R. Martin, B. Gély, L. Klein, D. Barredo, S. Geier, N.-C. Chiu, F. Grusdt, A. Bohrdt, T. Lahaye, and A. Browaeys, Realization of a doped quantum antiferromagnet with dipolar tunnelings in a rydberg tweezer array (2025), arXiv:2501.08233 [quant-ph].
- [57] E. Bobrow, K. Stubis, and Y. Li, Phys. Rev. B **98**, 180101 (2018).
- [58] S. R. White, Phys. Rev. Lett. **102**, 190601 (2009).
- [59] M. Yang and S. R. White, Phys. Rev. B **102**, 094315 (2020).
- [60] J. Haegeman, C. Lubich, I. Oseledets, B. Vandereycken, and F. Verstraete, Phys. Rev. B **94**, 165116 (2016).
- [61] J. Haegeman, J. I. Cirac, T. J. Osborne, I. Pižorn, H. Verschelde, and F. Verstraete, Phys. Rev. Lett. **107**, 070601 (2011).
- [62] G. Vidal, Phys. Rev. Lett. **91**, 147902 (2003).
- [63] S. R. White and A. E. Feiguin, Phys. Rev. Lett. **93**, 076401 (2004).
- [64] E. M. Stoudenmire and S. R. White, New Journal of Physics **12**, 055026 (2010).
- [65] N. Metropolis, A. W. Rosenbluth, M. N. Rosenbluth, A. H. Teller, and E. Teller, The Journal of Chemical Physics **21**, 1087 (1953).
- [66] W. K. Hastings, Biometrika **57**, 97 (1970).
- [67] K. K. Nielsen, Phys. Rev. B **108**, 085125 (2023).
- [68] S. A. Trugman, Phys. Rev. B **37**, 1597 (1988).
- [69] C. D. White, M. Zaletel, R. S. K. Mong, and G. Refael, Phys. Rev. B **97**, 035127 (2018).
- [70] S. Anand, C. D. White, J. Kemp, J. Wei, N. Y. Yao, and M. P. Zaletel, Efficient classical simulation of infinite-temperature operator dynamics beyond one-dimensional, local spin chains (to appear).
- [71] L. P. Kadanoff and P. C. Martin, Annals of Physics **24**, 419 (1963).
- [72] R. Steinigeweg, F. Heidrich-Meisner, J. Gemmer, K. Michielsen, and H. De Raedt, Phys. Rev. B **90**, 094417 (2014).
- [73] B. Kloss, Y. B. Lev, and D. Reichman, Phys. Rev. B **97**, 024307 (2018).
- [74] T. Rakovszky, C. W. von Keyserlingk, and F. Pollmann, Phys. Rev. B **105**, 075131 (2022).
- [75] P. Calabrese and A. Gambassi, Journal of Physics A: Mathematical and General **38**, R133 (2005).
- [76] A. Chandran, A. Nanduri, S. S. Gubser, and S. L. Sondhi, Phys. Rev. B **88**, 024306 (2013).
- [77] A. Maraga, A. Chiochetta, A. Mitra, and A. Gambassi, Phys. Rev. E **92**, 042151 (2015).
- [78] J. Feldmeier, P. Sala, G. De Tomasi, F. Pollmann, and M. Knap, Phys. Rev. Lett. **125**, 245303 (2020).
- [79] J. F. Rodriguez-Nieva, A. P. Orioli, and J. Marino, Proceedings of the National Academy of Sciences **119**, e2122599119 (2022).
- [80] M. Ljubotina, M. Žnidarič, and T. Prosen, Nature Communications **8**, 16117 (2017).
- [81] L. Katz, M. Guinan, and R. J. Borg, Phys. Rev. B **4**, 330 (1971).
- [82] N. Peterson, Journal of Nuclear Materials **69-70**, 3 (1978).
- [83] T. Ishikawa and R. B. McLellan, Journal of Physics and Chemistry of Solids **46**, 445 (1985).
- [84] H. Bonzel, Surface Science **21**, 45 (1970).
- [85] S. Fujita, Journal of Physics and Chemistry of Solids **49**, 41 (1988).
- [86] L. Onsager, Phys. Rev. **65**, 117 (1944).
- [87] E. Tarquini, G. Biroli, and M. Tarzia, Phys. Rev. B **95**, 094204 (2017).
- [88] B. V. Tiggelen, *Diffuse Waves in Complex Media*, edited by J.-P. Fouque (Springer, Dordrecht, 1999) Chap. Localization of waves.
- [89] U. Wolff, Phys. Rev. Lett. **62**, 361 (1989).
- [90] S. A. Trugman, Phys. Rev. B **41**, 892 (1990).
- [91] G. J. Dolan and D. D. Osheroff, Phys. Rev. Lett. **43**, 721 (1979).
- [92] B. L. Altshuler, A. G. Aronov, and P. A. Lee, Phys. Rev. Lett. **44**, 1288 (1980).
- [93] B. L. Altshuler, D. Khmel'nitzkii, A. I. Larkin, and P. A. Lee, Phys. Rev. B **22**, 5142 (1980).
- [94] H. Bruus and K. Flensberg, *Many-body quantum theory in condensed matter physics – an introduction* (Oxford University Press, 2016).

- [95] T. Guthardt, M. Scheb, J. von Delft, F. Grusdt, and A. Bohrdt, Finite-temperature real-time properties of magnetic polarons in two-dimensional quantum antiferromagnets (2025), arXiv:2504.07715 [cond-mat.quant-gas].
- [96] There are two minor differences between the investigated models, both of which should not lead to qualitative differences. (1) Ref. [95] includes a nearest-neighbor density-density term which arises in the large U/t limit of the Fermi-Hubbard model, which, however, leads to a fixed energy shift for a single dopant and thereby no differences in the dynamics. (2) The investigations in Ref. [95] is at lower spin couplings, $J/t < 1$.
- [97] A. E. Feiguin and S. R. White, Phys. Rev. B **72**, 220401 (2005).
- [98] P. M. Chaikin and T. C. Lubensky, Hydrodynamics, in *Principles of Condensed Matter Physics* (Cambridge University Press, 1995) p. 417–494.
- [99] M. Fishman, S. R. White, and E. M. Stoudenmire, SciPost Phys. Codebases , 4 (2022).
- [100] J. Hauschild and F. Pollmann, SciPost Phys. Lect. Notes , 5 (2018).
- [101] J. Hauschild, J. Unfried, S. Anand, B. Andrews, M. Bintz, U. Borla, S. Divic, M. Drescher, J. Geiger, M. Hefel, K. Hémery, W. Kadow, J. Kemp, N. Kirchner, V. S. Liu, G. Möller, D. Parker, M. Rader, A. Romén, S. Scalet, L. Schoonderwoerd, M. Schulz, T. Soejima, P. Thoma, Y. Wu, P. Zechmann, L. Zweng, R. S. K. Mong, M. P. Zaletel, and F. Pollmann, SciPost Phys. Codebases , 41 (2024).
- [102] A. Wietek, Y.-Y. He, S. R. White, A. Georges, and E. M. Stoudenmire, Phys. Rev. X **11**, 031007 (2021).

Appendix A: Fragmentation of t - J_z models

In this Appendix, we construct the symmetry operators that correspond to the Hilbert space fragmentation of spin-1/2 lattices with Ising interactions and 1D hopping. Moreover, we compute the number of Krylov subspaces and show that this scales exponentially in system size. In particular, this applies to models of the form

$$\hat{H} = - \sum_{\langle \mathbf{i}, \mathbf{j} \rangle_x, \sigma} t_{ij} \hat{\mathcal{P}} \left[\hat{c}_{i\sigma}^\dagger \hat{c}_{j\sigma} + \hat{c}_{j\sigma}^\dagger \hat{c}_{i\sigma} \right] \hat{\mathcal{P}} + \sum_{\mathbf{i}} J_{\mathbf{i}}^{(1)} \hat{S}_{\mathbf{i}}^z + \frac{1}{2} \sum_{\mathbf{i}, \mathbf{j}} J_{\mathbf{i}, \mathbf{j}}^{(2)} \hat{S}_{\mathbf{i}}^z \hat{S}_{\mathbf{j}}^z + \dots, \quad (\text{A1})$$

where the \dots indicate arbitrary higher-order Ising terms. The crucial part here is that the hopping cannot lead to any *loops* in the lattice and should only be to nearest neighbors. Here, we will take the particular case where the hopping is along one spatial direction, x , indicated by $\langle \mathbf{i}, \mathbf{j} \rangle_x$. The geometry of the lattice is otherwise completely general. Since there is no hopping across the legs of the lattice, y , it is clear that the number of spin- \uparrow and \downarrow in each leg is an integral of motion. I.e., $[\hat{N}_{y\sigma}, \hat{H}] = [\sum_x \hat{n}_{(x,y)\sigma}, \hat{H}] = 0$ for $\sigma = \uparrow, \downarrow$ and $\hat{n}_{(x,y)\sigma} = \hat{c}_{(x,y)\sigma}^\dagger \hat{c}_{(x,y)\sigma}$ the number of spin- σ at site

(x, y) . This gives in total $2 \times N_y$ integrals of motion.

Moreover, the arguments given in Sec. II mean that the *pattern* of the spins is unaltered in each leg of the lattice. To be more precise, we define the operators

$$\begin{aligned} \hat{S}_{1,y} &= \sum_{x_1=1}^{N_x} \hat{S}_{(x_1,y)}^z \prod_{x=1}^{x_1-1} [1 - \hat{n}_{(x,y)}], \\ \hat{S}_{2,y} &= \sum_{x_1=1}^{N_x} \hat{n}_{(x_1,y)} \prod_{x=1}^{x_1-1} [1 - \hat{n}_{(x,y)}] \sum_{x_2=x_1+1}^{N_x} \hat{S}_{(x_1,y)}^z \prod_{x=x_1+1}^{x_2-1} [1 - \hat{n}_{(x,y)}], \\ \hat{S}_{3,y} &= \dots \end{aligned} \quad (\text{A2})$$

for each leg y of the lattice. Here, the string $\prod_{x=1}^{x_1-1} [1 - \hat{n}_{(x,y)}]$ makes sure that there is only a nonzero contribution to the sum over x_1 at the position of the *first spin*. Writing an Ising eigenstate as $|\sigma\rangle = \prod_{\mathbf{i}} |\sigma_{\mathbf{i}}\rangle$, where $\sigma_{\mathbf{i}} = +1/2, 0, -1/2$ signifies a spin- \uparrow , a hole and a spin- \downarrow respectively, it follows that

$$\hat{S}_{l,y} |\sigma\rangle = \sigma_{x_l,y} |\sigma\rangle. \quad (\text{A3})$$

Here, x_l is the x -coordinate of the l th spin in leg y , i.e., the l th value of $\sigma_{\mathbf{i}}$ that is nonzero. In total, we can, thus, define N_x such operators. Moreover, because the Hamiltonian in Eq. (A1) can at most move the spins along the x -direction and *not alter their relative order*, it follows that

$$\begin{aligned} \hat{H} \hat{S}_{l,y} |\sigma\rangle &= \sigma_{x_l,y} \hat{H} |\sigma\rangle = \hat{S}_{l,y} \hat{H} |\sigma\rangle \Rightarrow \\ [\hat{H}, \hat{S}_{l,y}] |\sigma\rangle &= 0. \end{aligned} \quad (\text{A4})$$

Since the Ising eigenstates, $|\sigma\rangle$, define a *complete set of states*, it follows that $[\hat{H}, \hat{S}_{l,y}] = 0$. Since they also commute with $\hat{N}_{y\sigma}$, we can simultaneously diagonalize the Hamiltonian in terms of eigenstates of $\hat{N}_{y\sigma}$ and all the $\hat{S}_{l,y}$'s. Moreover, in a symmetry sector with $N_{y\uparrow}$ spin- \uparrow and $N_{y\downarrow}$ spin- \downarrow in leg y , there are $N_{y\uparrow} + N_{y\downarrow}$ nonzero eigenvalues $S_{l,y}$, $\{S_{1,y}, S_{2,y}, \dots, S_{N_{y\uparrow} + N_{y\downarrow}, y}, 0, \dots, 0\}$. Hence, for given $\{N_{y\uparrow}, N_{y\downarrow}\}_{y=1}^{N_y}$, there are

$$\prod_{y=1}^{N_y} \binom{N_{y\uparrow} + N_{y\downarrow}}{N_{y\uparrow}} \quad (\text{A5})$$

symmetry sectors. The total number of Krylov subspaces

is then

$$\begin{aligned}
K &= \sum_{\{N_{y\uparrow}, N_{y\downarrow}\}_{y=1}^{N_y}} \prod_{y=1}^{N_y} \binom{N_{y\uparrow} + N_{y\downarrow}}{N_{y\uparrow}} \\
&= \left[\sum_{\{N_{y\uparrow}, N_{y\downarrow}\}} \binom{N_{y\uparrow} + N_{y\downarrow}}{N_{y\uparrow}} \right]^{N_y} \\
&= \left[\sum_{N_{y\uparrow}=0}^{N_x} \sum_{N_{y\downarrow}=0}^{N_x - N_{y\uparrow}} \binom{N_{y\uparrow} + N_{y\downarrow}}{N_{y\uparrow}} \right]^{N_y} \\
&= \left[\sum_{N_{y\uparrow}=0}^{N_x} \binom{N_x + 1}{N_{y\uparrow} + 1} \right]^{N_y} = [2^{N_x+1} - 1]^{N_y}, \quad (\text{A6})
\end{aligned}$$

which is exponential in the total system size, $N = N_x \times N_y$. This established fragmentation [10]. Moreover, we can check that this decomposition also gives the full Hilbert space dimension. Indeed, for each leg, y , with quantum numbers $N_{y\uparrow}, N_{y\downarrow}$, the Krylov subspace has size

$$D(N_{y\uparrow}, N_{y\downarrow}) = D(N_{y\uparrow} + N_{y\downarrow}) = \binom{N_x}{N_{y\uparrow} + N_{y\downarrow}}. \quad (\text{A7})$$

The total Hilbert space dimensionality is then

$$\begin{aligned}
\dim(\mathcal{H}) &= \sum_{\{N_{y\uparrow}, N_{y\downarrow}\}_{y=1}^{N_y}} \prod_{y=1}^{N_y} \binom{N_x}{N_{y\uparrow} + N_{y\downarrow}} \binom{N_{y\uparrow} + N_{y\downarrow}}{N_{y\uparrow}} \\
&= \prod_{y=1}^{N_y} \sum_{\{N_{y\uparrow}, N_{y\downarrow}\}} \binom{N_x}{N_{y\uparrow} + N_{y\downarrow}} \binom{N_{y\uparrow} + N_{y\downarrow}}{N_{y\uparrow}} \\
&= \left[\sum_{\{N_{y\uparrow}, N_{y\downarrow}\}} \binom{N_x}{N_{y\uparrow} + N_{y\downarrow}} \binom{N_{y\uparrow} + N_{y\downarrow}}{N_{y\uparrow}} \right]^{N_y} \\
&= [3^{N_x}]^{N_y} = 3^{N_x N_y}. \quad (\text{A8})
\end{aligned}$$

This is, indeed, the total size of the Hilbert space, as each site has a three-dimensional Hilbert space, $|0\rangle, |\uparrow\rangle, |\downarrow\rangle$. Finally, for a single hole, say in leg $y = 0$, $N_{y=0\uparrow} + N_{y=0\downarrow} = N_x - 1$, whereas $N_{y\uparrow} + N_{y\downarrow} = N_x$. The total size of that Krylov subspace is, thus,

$$\begin{aligned}
\prod_{y=1}^{N_y} D(N_{y\uparrow} + N_{y\downarrow}) &= D(N_x - 1) = \binom{N_x}{N_x - 1} \\
&= \frac{N_x!}{(N_x - 1)! \cdot 1!} = N_x. \quad (\text{A9})
\end{aligned}$$

This is, indeed, what is indicated in Fig. 1. The first step comes from the fact that $D(N_x) = 1$.

Appendix B: Details on TEBD

In this Appendix, we give more details on how the TEBD calculations are carried out.

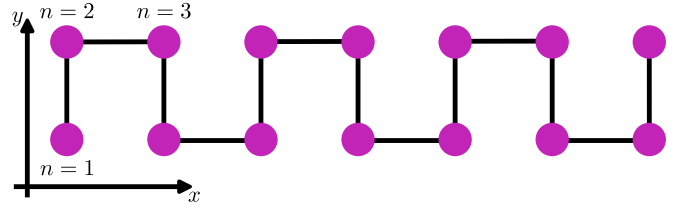


FIG. 11. (a) Illustration of how the sites are connected into a snake pattern, mapping the two-leg ladder to a one-dimensional chain, $n = 1, 2, 3, \dots$

To set up the TEBD algorithm, we follow Ref. [40]. To this end, we write the Hamiltonian as the sum of a leg (\parallel) and rung (\perp) Hamiltonian

$$\begin{aligned}
\hat{H} &= \hat{H}_{\perp} + \hat{H}_{\parallel} \\
\hat{H}_{\perp} &= \sum_{x=0}^{N_x-1} \hat{H}_{\perp,x}, \quad \hat{H}_{\parallel} = \sum_{y=0}^1 \sum_{x=0}^{N_x-2} \hat{H}_{\parallel,x}^{(y)} \quad (\text{B1})
\end{aligned}$$

Here, $\hat{H}_{\perp,x}$ is the local term that connects the two sites $(x, 0)$ and $(x, 1)$ on rung x , whereas $\hat{H}_{\parallel,x}^{(y)}$ connects the two sites $(x, y), (x+1, y)$ on leg y . Moreover, we map the two-leg ladder with dimension $N_x \times 2$ to a one-dimensional line as indicated in Fig. 11, typically referred to as snaking an MPS through the lattice. We then define the local Hamiltonian operators in this linear space ($n \in \{1, 2, \dots, 2N_x - 1\}$) as

$$\hat{H}_n = \begin{cases} \frac{1}{2} \hat{H}_{\perp, (n-1)/2}, & n \text{ odd}, \\ \hat{H}_{\parallel, n/2}^{(1)}, & n = 2 \pmod{4}, \\ \hat{H}_{\parallel, n/2}^{(0)}, & n = 0 \pmod{4}. \end{cases} \quad (\text{B2})$$

Note that we use *half* the rung coupling on the odd-numbered sites. The reason for this will be apparent shortly. Each time step of the TEBD is then performed by the following Trotterization. The first part consists of (step size $\delta\tau$)

$$\hat{U}(\delta\tau) = \prod_{n=1}^{2N_x-1} \exp[-i\hat{H}_n\delta\tau/2]. \quad (\text{B3})$$

In a linear chain, a TEBD time step then consists of [63] updating the wave function at time τ to $\tau + \delta\tau$ with the update, $|\psi(\tau + \delta\tau)\rangle = \hat{U}(\delta\tau)\text{Rev}[\hat{U}(\delta\tau)]|\psi(\tau)\rangle$, where $\text{Rev}[\cdot]$ reverses the order of the products. However, in the ladder we must take into account that some of the coupled sites are no longer along the line connecting the sites [Fig. 11]. Therefore, the total TEBD time step consists of the following sequence of operations

$$\begin{aligned}
|\psi(\tau + \delta\tau)\rangle &= \hat{U}(\delta\tau)\hat{S}\hat{U}(\delta\tau) \\
&\times \text{Rev}[\hat{U}(\delta\tau)\hat{S}\hat{U}(\delta\tau)]|\psi(\tau)\rangle \quad (\text{B4})
\end{aligned}$$

Here, the second part consists of (t - J type) SWAP operations on all rungs (i.e. odd n)

$$\hat{S} = \prod_{n \text{ odd}} \hat{S}_n. \quad (\text{B5})$$

The swapping of the fermions on the rungs, enable us to couple the sites along the ladder that were not coupled in the first operation of $\hat{U}(\delta\tau)$. Moreover, the second application of $\hat{U}(\delta\tau)$ after the SWAP explains why the Hamiltonian term for the rung part is cut in half in Eq. (B2). While all the Hamiltonian terms can straightforwardly be implemented in ITensor [99], the t - J type SWAP gates are not implemented beforehand. We do this by defining setting

$$\begin{aligned} \langle 00 | \hat{S}_n | 00 \rangle &= \langle 0\uparrow | \hat{S}_n | 0\uparrow \rangle = \langle 0\downarrow | \hat{S}_n | 0\downarrow \rangle = 1, \\ \langle \uparrow\uparrow | \hat{S}_n | \uparrow\uparrow \rangle &= \langle \downarrow\downarrow | \hat{S}_n | \downarrow\downarrow \rangle = -1, \end{aligned} \quad (\text{B6})$$

and using that $\hat{S}_n^\dagger = \hat{S}_n$. All other matrix elements are 0. This is then implemented as an ITensor operator of SiteType "tJ".

Appendix C: Details on METTS

In this Appendix, we give more details on how the METTS sampling of the spin background is performed, as well as an analysis of the autocorrelation time for the achieved samples.

For our METTS algorithm to sample the spin background, we use an imaginary time step of $\delta\beta = 0.05/J$. The algorithm starts from the Néel-ordered state

$$|\sigma_0\rangle = \left| \begin{array}{cccccccc} \uparrow & \downarrow & \uparrow & \downarrow & \uparrow & \downarrow & \uparrow & \downarrow \\ \downarrow & \uparrow & \downarrow & \uparrow & \downarrow & \uparrow & \downarrow & \uparrow \end{array} \dots \right\rangle. \quad (\text{C1})$$

The achieved METTS at each step, j , $|\phi(\sigma_j)\rangle \propto \exp[-\beta\hat{H}_J/2]|\sigma_j\rangle$ is collapsed in the \hat{S}^z eigen-basis for odd j , whereas it is collapsed in the orthogonal \hat{S}^x eigen-basis for even j . This is to minimize the sample-to-sample autocorrelation [64, 102] and also results in fluctuations in the S^z charge (the magnetization) of the sampled spin state. Moreover, we let the system thermalize by using 10 "warm-up" steps, which are not saved as samples. Finally, to minimize autocorrelation even further, we only keep every fourth sample, all of which are collapsed in the \hat{S}^z eigen-basis. In Fig. 12, we show the estimated autocorrelation function [102]

$$\rho[\hat{A}](l) = \frac{1}{|S| - l} \sum_{j=1}^{|S|-l} (A_j - \mathbb{E}[A])(A_{j+l} - \mathbb{E}[A]), \quad (\text{C2})$$

based on this sampling for the average energy per site, $\hat{A} = \hat{H}_J/N$, for the used $|S| = 100$ samples at two indicated inverse temperatures. Here, $A_j = \langle \phi_j | \hat{A} | \phi_j \rangle$ is the average of \hat{A} for step j , whereas $\mathbb{E}[A] = |S|^{-1} \sum_j^{|S|} A_j$ is the sample mean. We find no discernible correlations between the samples.

Appendix D: Magnetic energy fluctuations

In this Appendix, we calculate the magnetic energy fluctuations in a single dopant hopping event to qualitatively describe the spin anisotropy dependency of the

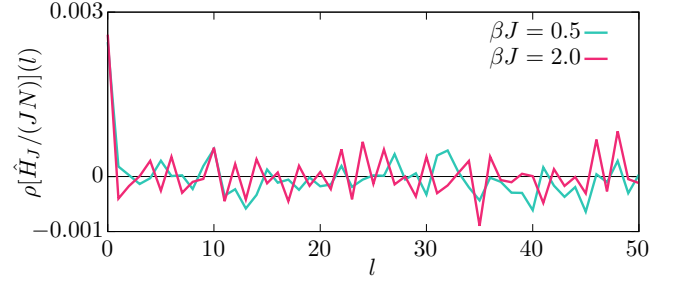


FIG. 12. Autocorrelation function [Eq. (C2)] for indicated inverse temperatures at $\alpha = 0.08$.

activation energy appearing in the Arrhenius relation for the diffusion coefficient.

We start from a state with a single hole at site $\mathbf{i} = (x, 0)$

$$\hat{\rho}_{\mathbf{i}} = \sum_{\sigma} \hat{c}_{\mathbf{i}\sigma} \hat{\rho}_J \hat{c}_{\mathbf{i}\sigma}^{\dagger}, \quad (\text{D1})$$

where $\rho_J = \exp[-\beta\hat{H}_J]/\text{tr}(\exp[-\beta\hat{H}_J])$ is the spin Gibbs state at inverse temperature β . Note that the state with a single dopant at the neighboring site $\mathbf{i} + \hat{x} = (x + 1, 0)$ can be achieved in the following manner

$$\hat{\rho}_{\mathbf{i}+\hat{x}} = \sum_{\sigma} \hat{c}_{\mathbf{i}+\hat{x}\sigma} \hat{\rho}_J \hat{c}_{\mathbf{i}+\hat{x}\sigma}^{\dagger} = \hat{V}^{\dagger} \hat{\rho}_{\mathbf{i}} \hat{V}, \quad (\text{D2})$$

with $\hat{V} = \hat{\mathcal{P}} \sum_{\sigma} \hat{c}_{\mathbf{i}+\hat{x}\sigma}^{\dagger} \hat{c}_{\mathbf{i}\sigma} \hat{\mathcal{P}}$ (remember that $\hat{\mathcal{P}}$ is the projection operator onto the subspace with at most one fermion per site). This means that the mean change in magnetic energy in a hopping event can be expressed as

$$\mu(\Delta E_J) = \text{tr}(\hat{\rho}_{\mathbf{j}} \hat{H}_J) - \text{tr}(\hat{\rho}_{\mathbf{i}} \hat{H}_J) = \text{tr}(\hat{\rho}_{\mathbf{i}} \Delta \hat{H}_J), \quad (\text{D3})$$

with $\Delta \hat{H}_J = \hat{V} \hat{H}_J \hat{V}^{\dagger} - \hat{H}_J$. One may check that $\text{tr}(\hat{\rho}_{\mathbf{j}} \hat{H}_J) = \text{tr}(\hat{\rho}_{\mathbf{i}} \hat{H}_J) = 0$ at $\beta = 0$, as the expressions depend on spin-spin correlators which vanish at infinite temperatures. Hence, the mean change in energy is also 0. Moreover, the rewriting in Eq. (D3) allows us to think of the hopping event as a transformation on the Hamiltonian, rather than on the state. It also means that we can straightforwardly express the *fluctuations* in the energy change as the variance of $\Delta \hat{H}_J$

$$\text{Var}(\Delta E_J) = \text{Var}(\Delta \hat{H}_J) = \text{tr}(\hat{\rho}_{\mathbf{i}} [\Delta \hat{H}_J - \mu(\Delta E_J)]^2). \quad (\text{D4})$$

Since \hat{V} moves a fermion from site \mathbf{i} to site $\mathbf{i} + \hat{x}$ (and \hat{V}^{\dagger} vice versa), it follows that $\hat{V} \hat{S}_{\mathbf{i}}^{\dagger} \hat{V}^{\dagger} = \hat{S}_{\mathbf{i}+\hat{x}}^{\dagger}$ and $\hat{V} \hat{S}_{\mathbf{i}+\hat{x}}^{\dagger} \hat{V}^{\dagger} = 0$ and leaves all other couplings unaltered. As a result,

$$\begin{aligned} \Delta \hat{H}_J &= \hat{H}_J(\mathbf{i} - \hat{x}, \mathbf{i} + \hat{x}) + \hat{H}_J(\mathbf{i} + \hat{y}, \mathbf{i} + \hat{x}) \\ &\quad - \sum_{\mathbf{j} \in \text{NN}(\mathbf{i} + \hat{x})} \hat{H}_J(\mathbf{j}, \mathbf{i} + \hat{x}), \end{aligned} \quad (\text{D5})$$

where $\hat{H}_J(\mathbf{i}, \mathbf{j}) = J[S_{\mathbf{i}}^z S_{\mathbf{j}}^z + \alpha(S_{\mathbf{i}}^x S_{\mathbf{j}}^x + S_{\mathbf{i}}^y S_{\mathbf{j}}^y)]$, and $\text{NN}(\mathbf{j})$ are the set of sites that are nearest neighbors to \mathbf{j} . At

infinite temperatures (where $\mu(\Delta E_J) = 0$), we may then write Eq. (D4) as

$$\begin{aligned} \text{Var}(\Delta E_J) &= \text{tr}(\hat{\rho}_{\mathbf{i}}[\hat{H}_J(\mathbf{i} - \hat{x}, \mathbf{i} + \hat{x})]^2) \\ &\quad + \text{tr}(\hat{\rho}_{\mathbf{i}}[\hat{H}_J(\mathbf{i} + \hat{y}, \mathbf{i} + \hat{x})]^2) \\ &\quad + \sum_{\mathbf{j} \in \text{NN}(\mathbf{i} + \hat{x})} \text{tr}(\hat{\rho}_{\mathbf{i}}[\hat{H}_J(\mathbf{j}, \mathbf{i} + \hat{x})]^2). \end{aligned} \quad (\text{D6})$$

Here, we use that only the quadratic terms give a nonzero contribution, because the rest will depend on spin-spin correlator that are zero at infinite temperature. This also means that four of the five terms above (there are three terms in the sum over \mathbf{j}) give exact the same contribution. The fifth and last one depends on $\hat{H}_J(\mathbf{i}, \mathbf{i} + \hat{x})$ and does

not contribute, because there is a hole at site \mathbf{i} in the state $\hat{\rho}_{\mathbf{i}}$. Finally, it is only terms that are quadratic in the spin operators on each site. Therefore,

$$\begin{aligned} \text{Var}(\Delta E_J) &= 4\text{tr}(\hat{\rho}_{\mathbf{i}}[\hat{H}_J(\mathbf{i} - \hat{x}, \mathbf{i} + \hat{x})]^2) \\ &= 4J^2 \left(\text{tr}(\hat{\rho}_{\mathbf{i}}[\hat{S}_{\mathbf{i}-\hat{x}}^z \hat{S}_{\mathbf{i}+\hat{x}}^z]^2) \right. \\ &\quad \left. + \alpha^2 \left[\text{tr}(\hat{\rho}_{\mathbf{i}}[\hat{S}_{\mathbf{i}-\hat{x}}^x \hat{S}_{\mathbf{i}+\hat{x}}^x]^2) + \text{tr}(\hat{\rho}_{\mathbf{i}}[\hat{S}_{\mathbf{i}-\hat{x}}^y \hat{S}_{\mathbf{i}+\hat{x}}^y]^2) \right] \right) \\ &= 4J^2 \left(\frac{1}{16} + \alpha^2 \left[\frac{1}{16} + \frac{1}{16} \right] \right) = \frac{J^2}{16} [1 + 2\alpha^2]. \end{aligned} \quad (\text{D7})$$

Taking the square root yields the standard deviation $\text{std}[\Delta E_J] = J[1 + 2\alpha^2]^{1/2}/2$ of the magnetic energy fluctuations, which is used in Sec. V C.